5-2014

Investigating Water Ice in Persistently Shadowed Craters in Mercury's North Polar Region

Ariel N. Deutsch
College of William and Mary

Recommended Citation

Deutsch, Ariel N., "Investigating Water Ice in Persistently Shadowed Craters in Mercury's North Polar Region" (2014). *Undergraduate Honors Theses.* Paper 55.
https://scholarworks.wm.edu/honorstheses/55

Investigating Water Ice in Persistently Shadowed Craters in Mercury's North Polar Region

A thesis submitted in partial fulfillment of the requirements for the degree of Bachelor of Science in Geology from the College of William and Mary in Virginia

By

Ariel N. Deutsch

Accepted for High Honors
(Honors, High Honors)

Dr. Christopher Bailey, Director

Dr. Joel Levine

Heather Macdonald
Dr. Heather Macdonald

Dr. Eugene Tracy

Williamsburg, VA
May 2014

Table of Contents

List of Figures....................3
List of Tables....................5
Abstract....................6
Introduction....................7
Background....................9
Previous Work....................17
Geologic Setting....................21
Methods....................24
    Imaging Details....................24
    Individual Crater Analysis....................25
    Regional Analysis....................29
Results....................31
    Individual Crater Results....................31
    Regional Results....................53
Discussion....................57
Conclusion....................70
Acknowledgements....................73
References....................74
Tables....................82
Appendices....................86
    Appendix A: MESSENGER's Payload....................86
    Appendix B: Explanation of MESSENGER Acronyms....................87
    Appendix C: ISIS3 Tools Used....................88

List of Figures

1. Study Area 8
2. Radar-Bright Regions on Mercury's North Pole 10
3. North Pole Temperature Conditions 11
4. North Pole Illumination Conditions 12
5. Ice Concentrations Preventing Neutron Escape 13
6. Medium- and High-Speed Neutron Data 14
7. Mercurian Surface Reflectivity Data 15
8. Lag Deposits Insulating Water Ice 17
9. Radar-Bright Deposits and Persistently Shadowed Craters in the North Polar Region 18
10. Persistently Shadowed Craters in the North Polar Region 19
11. Crustal Thickness of Mercury 22
12. Individually Investigated Craters 32
13. Relationship between Central Latitude and Crater Diameter for Craters with and without Dark Material 33
14. Re-Classified Individually Investigated Craters 34
15. Relationship between Central Latitude and Crater Diameter for Re-classified Craters with and without Dark Material 35
16. Dark Material and Persistent Shadow of Unnamed A Crater 36
17. Dark Material and Persistent Shadow of Unnamed B Crater 36
18. Dark Material, Radar-Bright Material, and Persistent Shadow of Unnamed C Crater....................37
19. Dark Material, Radar-Bright Material, and Persistent Shadow of Berlioz 38
20. Dark Material, Radar-Bright Material, and Persistent Shadow of Unnamed D Crater 38
21. Dark Material, Radar-Bright Material, and Persistent Shadow of Unnamed E Crater....................39
22. Dark Material, Radar-Bright Material, and Persistent Shadow of Unnamed F Crater 40
23. Dark Material, Radar-Bright Material, and Persistent Shadow of Unnamed G Crater 40
24. Dark Material, Radar-Bright Material, and Persistent Shadow of Unnamed H Crater 41
25. Dark Material, Radar-Bright Material, and Persistent Shadow of Ensor Crater 41
26. Dark Material, Radar-Bright Material, and Persistent Shadow of Unnamed I Crater....................42
27. Dark Material, Radar-Bright Material, and Persistent Shadow of Remarque Crater 42
28. Dark Material, Radar-Bright Material, and Persistent Shadow of Unnamed J Crater....................43
29. Dark Material, Radar-Bright Material, and Persistent Shadow of Unnamed K Crater 44

30. Dark Material, Radar-Bright Material, and Persistent Shadow of Unnamed L Crater...........44
31. Dark Material, Radar-Bright Material, and Persistent Shadow of Unnamed M Crater..........45
32. Dark Material, Radar-Bright Material, and Persistent Shadow of Varma..............................46
33. Dark Material, Radar-Bright Material, and Persistent Shadow of Unnamed N Crater 46
34. Dark Material, Radar-Bright Material, and Persistent Shadow of Unnamed O Crater 47
35. Dark Material, Radar-Bright Material, and Persistent Shadow of Unnamed P Crater...........48
36. Dark Material, Radar-Bright Material, and Persistent Shadow of Unnamed Q Crater 48
37. Dark Material, Radar-Bright Material, and Persistent Shadow of Unnamed R Crater...........49
38. Dark Material, Radar-Bright Material, and Persistent Shadow of Unnamed S Crater...........50
39. Dark Material, Radar-Bright Material, and Persistent Shadow of Unnamed T Crater...........50
40. Dark and Light Material, Radar-Bright Material, and Persistent Shadow of Prokofiev..........51
41. Dark Material, Radar-Bright Material, and Persistent Shadow of Unnamed U Crater 52
42. Dark Material, Radar-Bright Material, and Persistent Shadow of Unnamed V Crater 52
43. Light Material, Radar-Bright Material, and Persistent Shadow of Kandinsky.......................53
44. Regions of Persistent Shadow..55
45. Regions with Radar-Bright Deposits 56
46. Comparison between Persistently Shadowed and Radar-Bright Regions 57
47. Mercurian polar surface and subsurface temperatures..67
48. Calculated water ice depths in North Polar Region 69

List of Tables

1. Craters with definite dark material 82
2. Craters with possible dark material..82
3. Craters with no visible dark material..83
4. Craters from poor images, preventing any dark material interpretations 83
5. Re-classified craters with definite dark material 84
6. Re-classified craters with definite dark material 84
7. Craters with light material 85

Abstract

Through a combination of Earth-based radar observations, available spacecraft neutron spectrometer and laser altimeter data, and thermal modeling, it has previously been suggested that the planet Mercury hosts extensive water ice deposits in its polar regions. This study concentrates on observations of the permanently shadowed craters of Mercury's north polar region, where water ice is expected. To examine the interior of craters that host radar-bright material, images from the Wide Angle Camera (WAC) aboard the Mercury Surface, Space Environment, Geochemistry, and Ranging (MESSENGER) spacecraft were processed using Integrated Software for Imagers and Spectrometers (ISIS) and stretched on a grayscale to expose reflectivity differences and surface features. This process revealed intriguing dark material within 53.2% of the individual craters studied in the region 75º N and northward, which is interpreted to be sublimation lags. The relationships between visible reflectivity material, radar-bright deposits, and regions of persistent shadow were mapped for these craters. Reflectivity-light material was revealed in the Prokofiev and Kandinsky craters (4.2%), indicating exposed water ice deposits. The remaining craters either did not reveal dark or light material (29.8%) or did not return images of high enough quality for analysis (12.8%). Additionally, the area of 84º N and northward was analyzed on a regional scale. Areas of persistent shadow were mapped and then compared to radar data to both qualify and quantify the relationship between shadowed areas and radar-bright features. In the study area, ~82% of the *Harmon et al.* (2011) radar-bright features aligned with the mapped areas of persistent shadow. The results of this study indicate that water ice stably resides in the persistently shadowed craters on Mercury's north polar region and is typically insulated by a reflectivity-dark lag deposit.

Introduction

The concept of water ice on other planets in the Solar System is an exciting one. Investigating water ice is important for understanding the geological, climatic, and potentially exobiological evolution of these bodies, and their Solar System at large. Water ice is known to reside on the polar caps of Mars as well as on some of Jupiter's and Saturn's moons (Bibring et al., 2004; Poirier, 1982). Now there is evidence for water ice on the innermost planet, as well.

There is considerable support for the hypothesis that Mercury is a host to abundant water ice in its permanently shadowed polar craters. First, radar data acquired by the Arecibo Observatory denote radar-bright deposits on Mercury's north polar region that show the same radar signature expected of pure water ice (Harmon et al., 2011). The larger polar deposits are located on the floors and walls of impact craters. Deposits that lie farther from the pole tend to concentrate on north facing crater walls (Chabot et al., 2013). Second, data from the Mercury Surface, Space Environment, Geochemistry, and Ranging (MESSENGER) spacecraft have supported the hypothesis. Data from the neutron spectrometer, which has measured average hydrogen concentrations within Mercury's radar-bright regions, indicate regions in the polar region that have both exposed and buried ice deposits (Lawrence et al., 2013). Finally, thermal models suggest that the polar regions of Mercury are indeed thermally stable enough to host stable water ice on a long-term time scale (Paige et al., 2013).

Craters in Mercury's North Pole have regions that are in persistent shadow, detected by mapping the areas that are never in light in each available image that has been relayed from MESSENGER. These areas of persistent shadow are sufficiently thermally stable to host persistent water ice (Paige et al., 2013). This research aims to determine the regions of shadow on Mercury for the area north of 84º N (Fig. 1). Previous work on this subject was conducted with just one year of MESSENGER orbital data, when coverage near the North Pole was incomplete (Chabot et al., 2013).

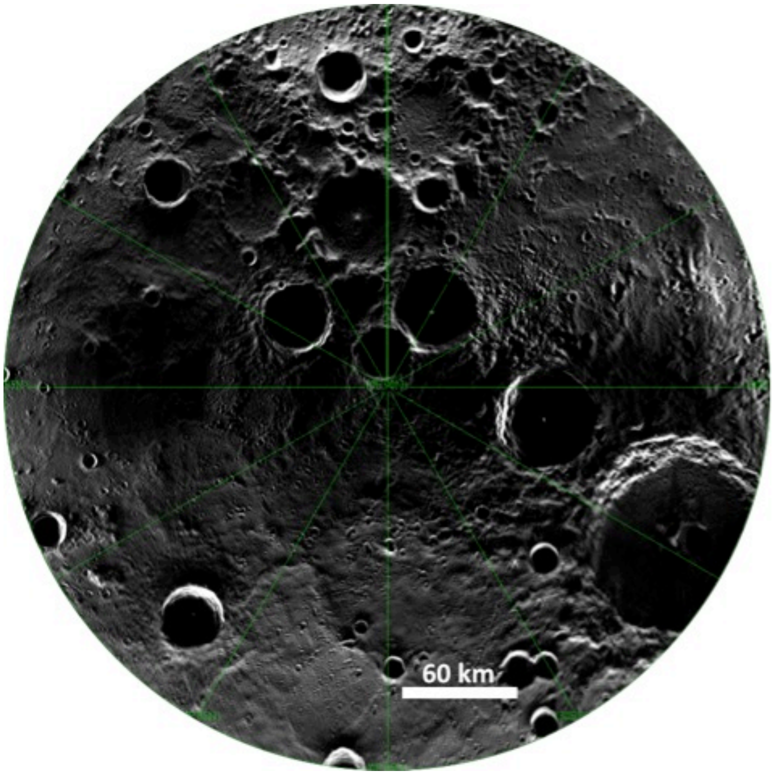

Figure 1. The study area of 84º N and northward on Mercury was delineated because previous research on radar-bright regions in persistently shadowed craters was conducted at a time when coverage of the North Pole was incomplete.

While areas of radar-bright material do indicate water ice, these areas are commonly reflectivity dark, indicating that they are not fully exposed at the surface (Neumann et al., 2013). It is most likely that water ice instead lies beneath a thin layer of organics (Paige et al., 2013). My research looks at where an organic-rich deposit insulates surface ice and where it does not, leaving the ice exposed at the surface.

In addition, I worked to compile a map of Mercury for the region of 84º N and northward to illustrate what areas are persistently shadowed. In addition to this regional-scale analysis, individual craters located 75º N and northward were investigated. These areas were then compared to radar data to both qualify and quantify the relationship between shadowed areas and radar-bright features. Reflectivity data overlain on the map was used to investigate what reflectivity features in these regions indicate about surface material. Determining the relationship between these variables helps to establish where water ice resides on Mercury and to what extend it is exposed at the planet's surface.

Background

Mercury has been referred to as the key to terrestrial planet evolution because of its extreme properties. While it possesses some of the most extreme properties of the rocky planets, Mercury is the least explored. MESSENGER was developed to explore this end member planet, which would lead to further insight on the formation and evolution of the other terrestrial planets. MESSENGER was launched in 2004 and completed one flyby of Earth, two flybys of Venus, and three flybys of Mercury before becoming the first spacecraft to orbit Mercury in 2011. This voyage yielded the first sets of new Mercury data since Mariner 10, which launched in 1973. The MESSENGER mission defined six primary science questions, managed by principal investigator Sean Solomon, to help develop the mission plan and the spacecraft's payload (Appendix A): 1) Why is Mercury so dense? 2) What is the geologic history of Mercury? 3) What is the nature of Mercury's magnetic field? 4) What is the structure of Mercury's core? 5) What are the unusual materials at Mercury's poles? 6) What volatiles are important at Mercury? This research focuses on the fifth science objective.

Mercurian radar imaging in 1991-1992 at Goldstone/Very Large Array and Arecibo Observatory indicated radar-bright material on the poles similar to data from the Mars' south polar cap and the three icy Galilean satellites, suggesting polar ice resides on Mercury (Fig. 2, Harmon et al., 2001). High-resolution imaging with the Arecibo S-band radar during 1999-2005 has been utilized to survey Mercury's polar ice deposits. Radar data acquired by the Arecibo Observatory indicates that polar deposits on Mercury show the same radar signature expected of pure water ice (Harmon et al., 2011). When radar data is overlain on a mosaic of Mercury's north polar region, the larger polar deposits align with the spatial configuration of impact craters (Fig. 2). In addition, impact craters farther from the North Pole show radar data concentrated on north-facing walls.

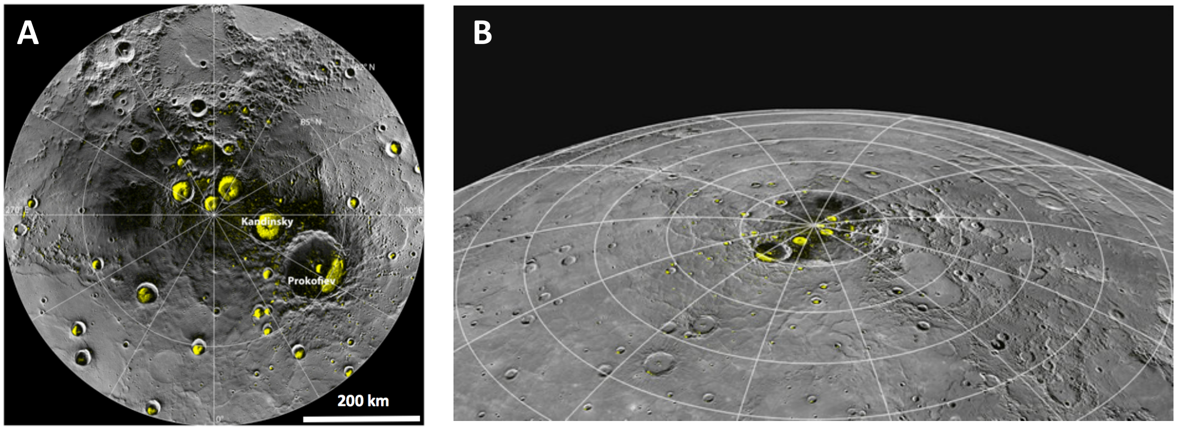

Figure 2. A: Data from the Arecibo Observatory indicates regions of high radar reflectivity in yellow superposed on a polar stereographic mosaic of the North Pole. These areas have the same radar signature expected from water ice. Radar-bright material tends to occur on the floors or walls of impact craters. High-latitude deposits farther from the North Pole tend to have radar-bright material concentrated on the north-facing walls, where the sunlight does not directly strike. **B:** A perspective view of the north polar region highlights the radar-bright deposits in yellow (Chabot et al., 2012).

Thermal modeling studies demonstrate that polar regions of Mercury are cold enough to support water ice (Fig. 3).

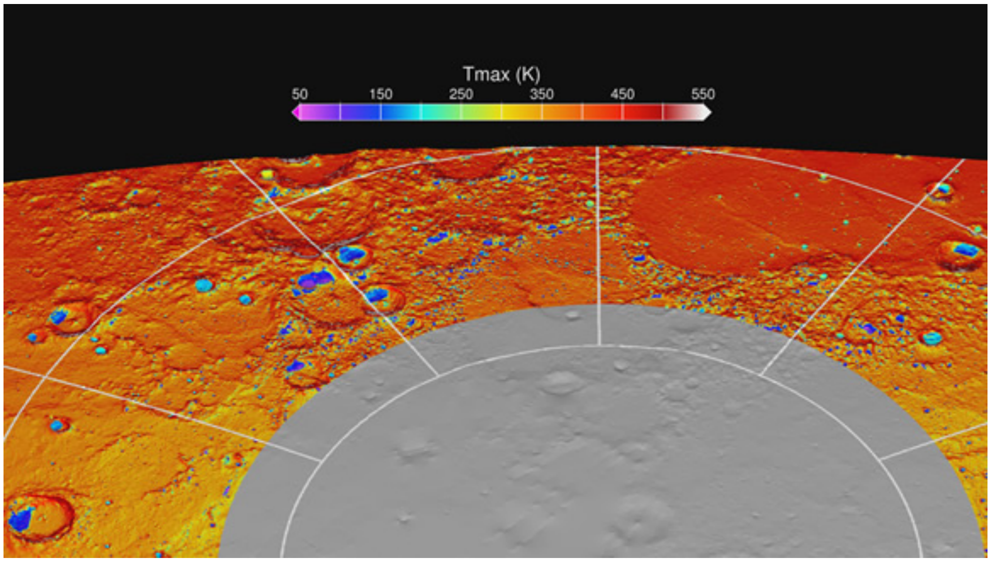

Figure 3. The maximum surface temperatures reached over a 2-year period are shown for the north polar region of Mercury. The thermal calculations are derived from measurements of Mercury's topography from the Mercury Laser Altimeter. Mercury shows greater surface temperature fluctuations than any other planet. Equatorial regions that receive direct sunlight reach up to 700 K, polar craters in persistent shadow can reach temperatures below 50 K. Temperatures below 112 K are thermally stable to support water ice over billion-year timescales (Paige et al., 2013).

The temperatures of flat, low-reflectivity polar surfaces are expected to remain below 167 K (Paige et al., 1992). With a small enough solar elevation angle, water ice could be supported on flat surfaces (Ingersoll et al., 1992). With low albedo measurements of A = 0.75, temperatures can exist below 120 K in these areas (Ingersoll et al., 1992). Within polar impact craters, surface temperatures in permanently shadowed regions are expected to be significantly lower, reaching 60 K (Paige et al., 1992). At temperatures below 112 K, pure water ice is stable against evaporation on a time scale of billions of years (Salvail and Fanale, 1994). Therefore, shadowed polar craters are thermally capable of hosting persistent water ice (Fig. 4).

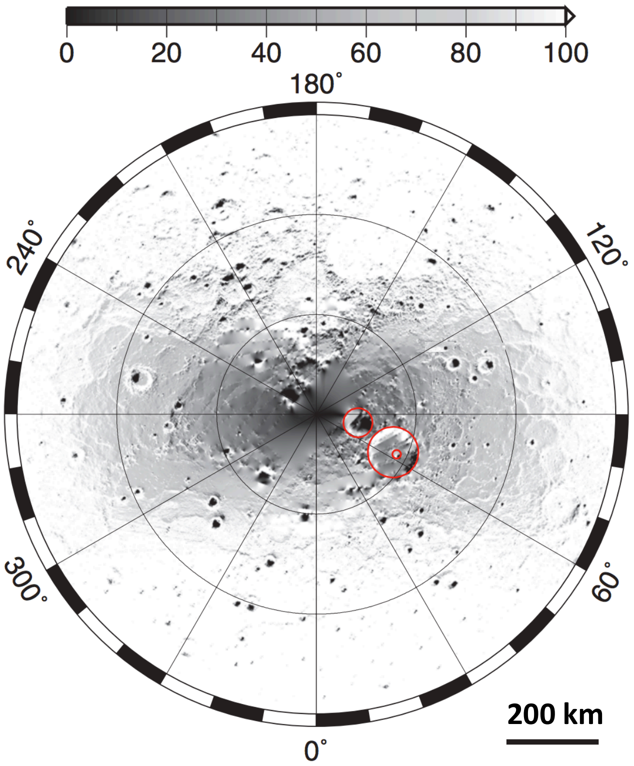

Figure 4. The maximum incident solar flux is shown over a 10-year period as a percentage of the solar constant at 1 astronomical unit from an illumination model. These values represent the incoming energy from solar radiation. Black areas indicate regions that do not receive sunlight. The craters Kandinsky and Prokofiev are outlined in red for orientation (Neumann et al., 2013).

The neutron data also indicates water ice in the polar regions of Mercury. MESSENGER uses neutron spectroscopy to map variations in epithermal, thermal, and fast neutrons emitted by Mercury's surface when struck by cosmic rays. Water ice concentrations are derived from average hydrogen concentrations within radar-bright regions are investigated. When galactic cosmic rays strike the planet's surface, neutrons are liberated from atomic nuclei in near-surface matter. The Neutron Spectrometer can then detect these escaped neutrons.

Hydrogen atoms prevent neutrons from escaping into space, which causes the spectrometer to obtain a lower relative flux in neutron readings (Fig. 5).

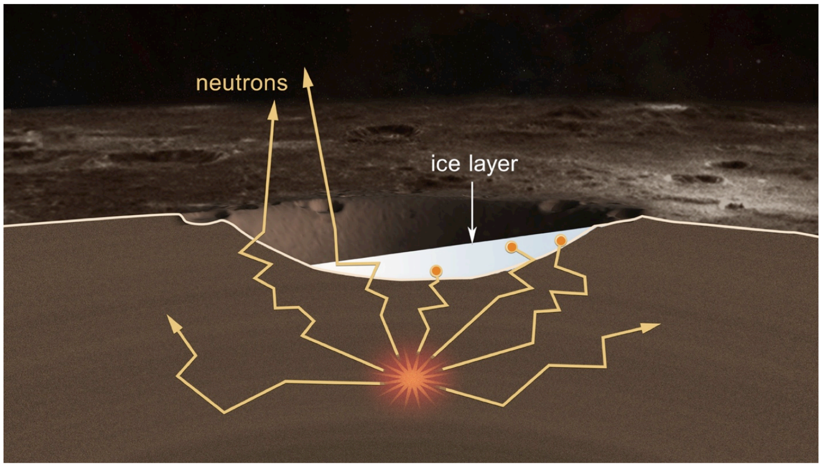

Figure 5. A meter-thick ice deposit is represented in white. When a galactic cosmic ray strikes the surface and liberates neutrons, this hydrogen-rich layer prevents the neutrons from escaping. A decrease in the rate of neutron detection is the signature of enhanced hydrogen concentrations, indicating water ice (Lawrence, 2012).

When a slab of water ice insulates the surface, the abundant hydrogen atoms result in a decrease in the rate of detected neutrons (Lawrence, 2012). Figure 6a shows data from medium-speed, epithermal neutrons with northern latitudes represented on the x-axis and the relative flux of neutron readings on the y-axis. The white line represents an outcome where there is no ice in radar-bright regions, thus there is no change in relative number of neutrons per given time with latitude. The blue line represents an outcome where all radar-bright regions consist of a thick layer of pure water ice. The MESSENGER data closely follow the blue line, which represents the simulation where all radar-bright regions have a thick layer of pure water ice. These data show that Mercury's polar regions have enhanced hydrogen concentrations, consistent with those of pure water ice, in its deposits.

High-speed neutron data support the medium-speed neutron data with measurements of water ice burial depth. Thick water ice deposits are likely insulated by a thinner surface of a less hydrogen-rich material. Figure 6b shows data from high-speed neutrons with northern latitudes again represented on the x-axis and the relative flux of neutron readings on the y-axis. The white line again represents an outcome where radar-bright regions lack ice. The blue line now represents an outcome where all radar-bright regions consist of pure water ice that is exposed at the planet's surface. The MESSENGER data closely follow the blue line until the upper northern latitudes, where it levels at a relative flux value between the white and blue lines. The decrease in neutron flux toward the North Pole is less than expected if water ice were exposed in all radar-bright regions, suggesting that most of the water ice in this area is buried. The ice was calculated to lie beneath a 10-20 cm thick layer of low-hydrogen material.

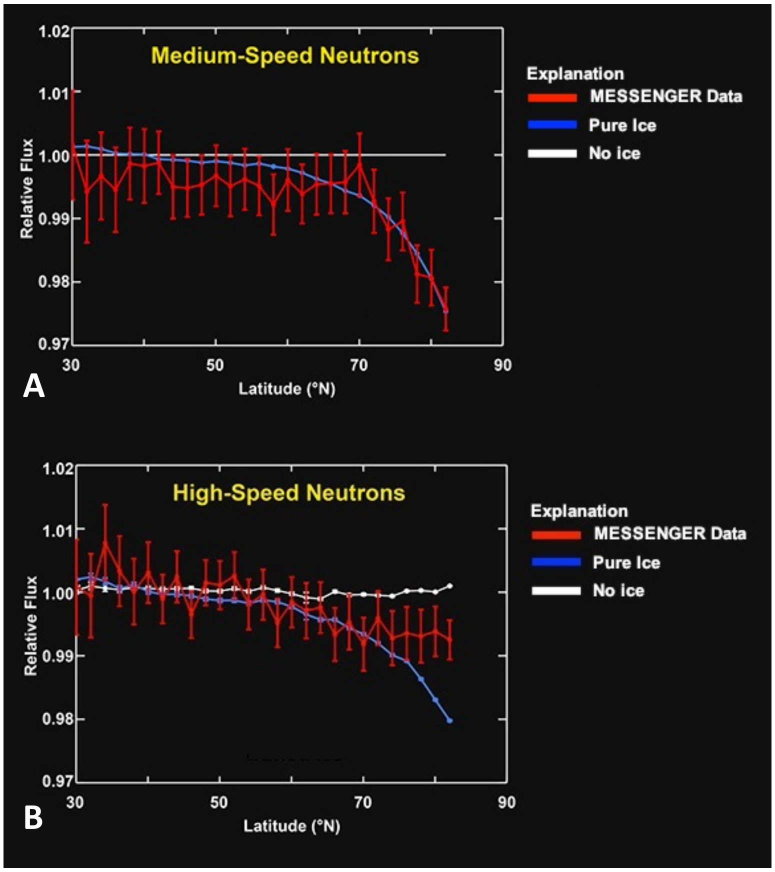

Figure 6. A: MESSENGER neutron spectrometer data from medium-speed neutrons in units of normalized counts per second averaged over 2º-wide latitude bins are plotted for the northern hemisphere as a function of latitude, from 30º N to the pole. Counts are normalized at an altitude of 400 km to the mean count rate of 60 cps. The error bars in each latitude bin represent twice the measured standard deviation of the mean. Mercury's data are juxtaposed with theoretical returns from a surface that shows no hydrogen atoms in white and one that has 100-weight % water ice in blue. **B:** MESSENGER neutron spectrometer data from high-speed neutrons, plotted on the same scale as above with the same additional data sets. Counts are now normalized at an altitude of 400 km to the mean count rate of 10 cps (Modified from Lawrence, 2012).

Data from the Mercury Laser Altimeter (MLA) shows that radar-bright polar regions are often reflectivity-dark, meaning they contain material of unusually low reflectance (Fig. 7). Exposed surface ice would show areas that are reflectivity-bright, that have a higher reflectance than the regional average. The majority of the radar-bright deposits are reflectivity-dark, suggesting that most of the permanent ice on Mercury is not exposed on the planet's surface. It has been suggested that a dark layer of organics insulates the ice, stabilizing it to higher temperatures and protecting it from thermal loss (Neumann et al, 2013).

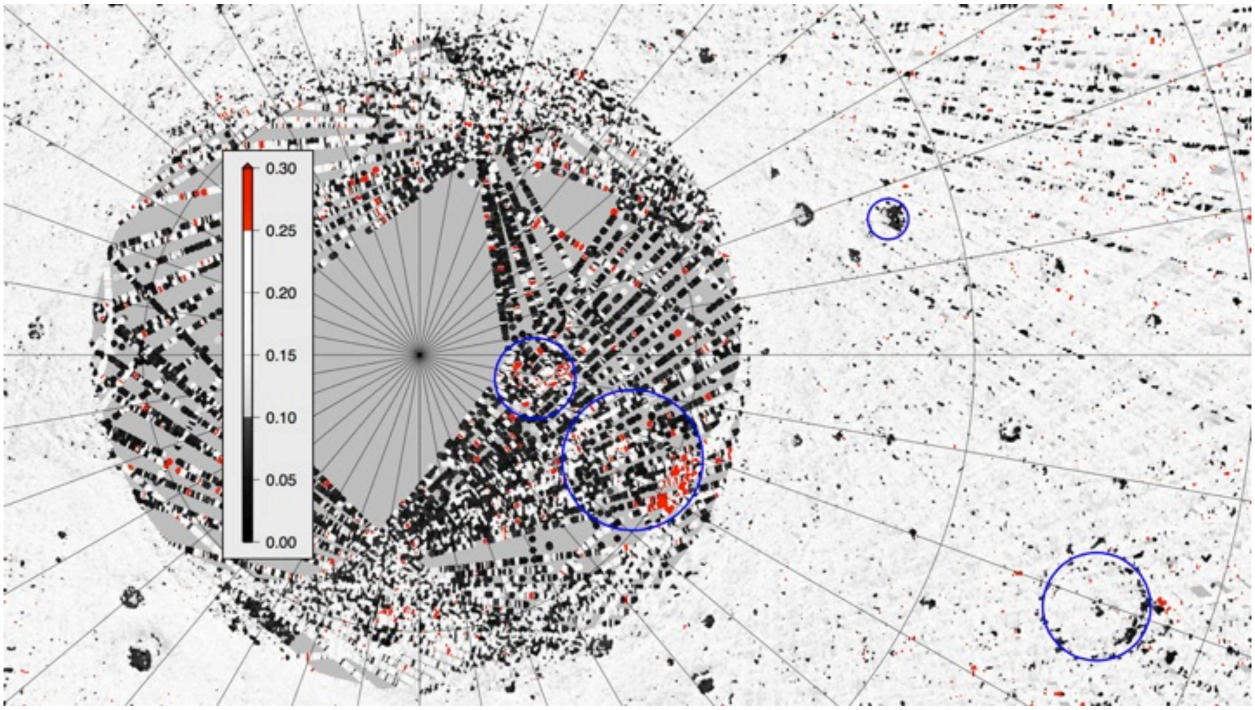

Figure 7. Surface reflectivity measurements are displayed for the north polar region. Measurements are relative to perfect Lambertian scattering and were taken by the Mercury Laser Altimeter from profiles taken at incidence angles below 30º from nadir. Any regions with no current data within 2 km are shaded gray. Red represents areas with greater than 50% higher reflectance values than the regional average, suggesting surface exposures of water ice. Black denotes regions of low reflectance, approximately half that of the typical surface, suggesting an insulating material atop water ice. Values are calculated as nearest-neighbor averages (Modified from Neumann, 2012).

Furthermore, there are craters in Mercury's north polar region that host water ice in regions that experience temperatures theoretically too warm to preserve surface ice, even in permanent shadow (Harmon et al., 2011). These conditions result from indirect heating by reflected and reradiated sunlight. These craters likely host ice that is not directly exposed at the planet's surface, but instead that is insulated by a thin dust mantle. Data from the Goldstone X-band radar imagery indicate environments capable of hosting stable water ice may be dependent on a reflectivity wavelength that could be consistent with that returned by an organic-rich dust mantle.

The geometry of impact craters creates a distinct illumination gradient. The angled rays of the Sun strike the south-facing walls of high-latitude craters, generating warm temperatures on the illuminated rim. Lower temperatures are characteristic of the crater's illuminated floor and the lowest temperatures are found on the other side of the crater in regions of permanent shadow. Lag deposits form when a comet or water-rich asteroid containing organic compounds strikes the planet's surface (Paige et al., 2013). The organic compounds and water disperse, and can migrate to the poles and become cold-trapped as ices (Paige et al., 2013). As the water in warmer regions vaporizes over time, the more stable organic compounds are left behind on the surface (Paige et al., 2013). Eventually the ice retreats into a stable long-term configuration. The organic impurities lay above the ice on the surface (Fig. 8).

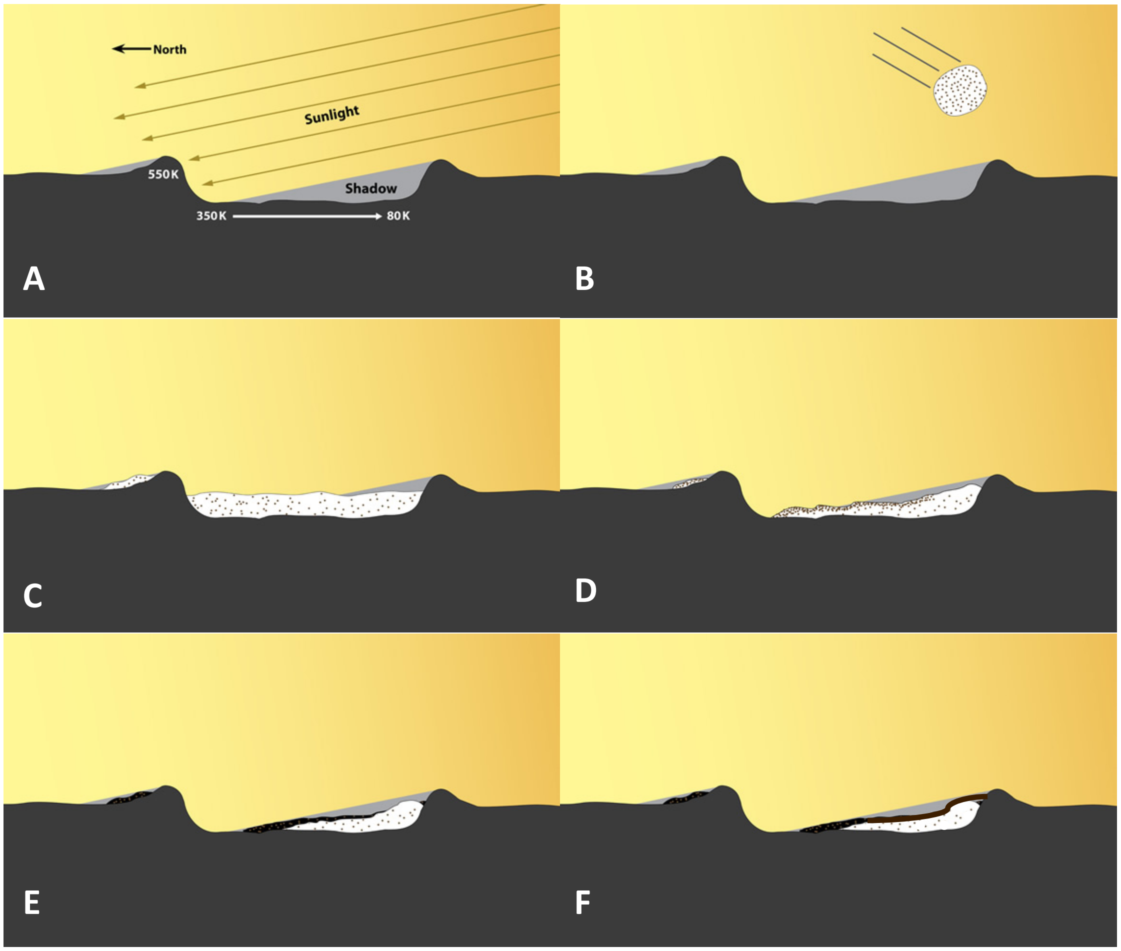

Figure 8. **A:** A typical crater cross-section is shown at high latitudes with the angled rays of the Sun striking the south-facing wall, creating an area of warm temperatures. The north-facing wall is not illuminated; the shadow yields colder temperatures. **B:** A comet or water-rich asteroid enters the region, composed of water and organic compounds. **C:** The impactor strikes the surface and its materials are spread across the region. The water and organics can become cold-trapped as ices. **D:** Water ice in the warmer regions vaporizes over time, leaving behind the more stable organic impurities. **E:** The ice deposit retreats further into a stable, long-term configuration. In the coldest regions, it is thermally stable to host the water ice on the surface. **F:** In warmer regions, the ice is completely covered by a dark layer of organics (Modified from Paige, 2012).

Previous Work

Earlier studies have investigated the relationship between radar-bright regions of Mercury's poles and areas of persistent shadow, derived from MESSENGER images (Chabot et al, 2012). They have shown qualitatively the exceptional agreement between impact crater and radar-bright deposit distribution (Fig. 9).

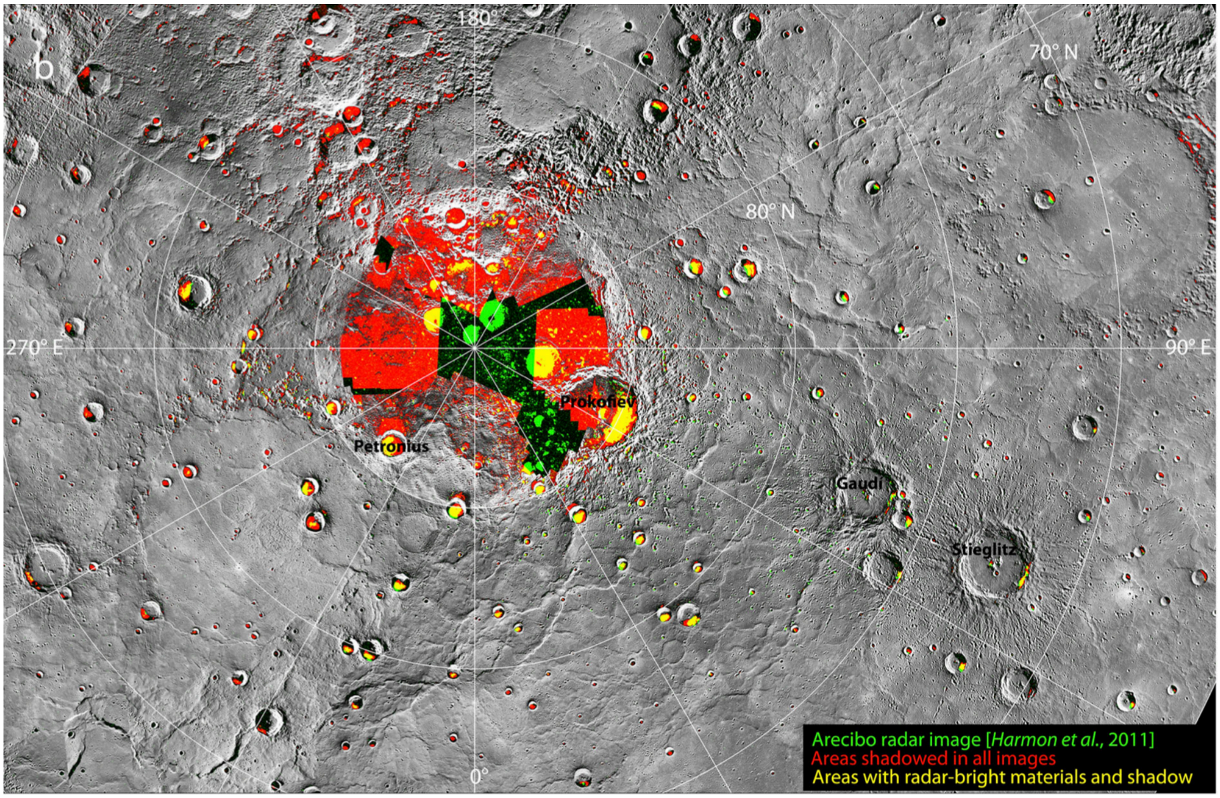

Figure 9. Radar-bright deposits derived from Arecibo Earth-based radar imagery are highlighted in green. Areas that are in persistent shadow are highlighted in red. When areas have radar-bright material within regions of persistent shadow, the intersection is marked with yellow. The region closest to the pole is shaded in black because global imagery coverage was not complete at the time of this study (Chabot et al., 2012).

A quantitative analysis concluded that approximately 70% of radar-bright deposits in the region 65º N to 85º N correspond to areas of persistent shadow. The remaining 30% of radar-bright deposits fall either within 4 km of shadowed areas or within the interiors of small craters (Chabot et al., 2012). Radar data is only accurate to about 2 km (Harmon et al., 2011) and MDIS mosaics can have an offset of nearly 1.8 km (Becker et al., 2012). Out of the 305 shadowed craters mapped, 92 also host radar-bright deposits (Fig. 10).

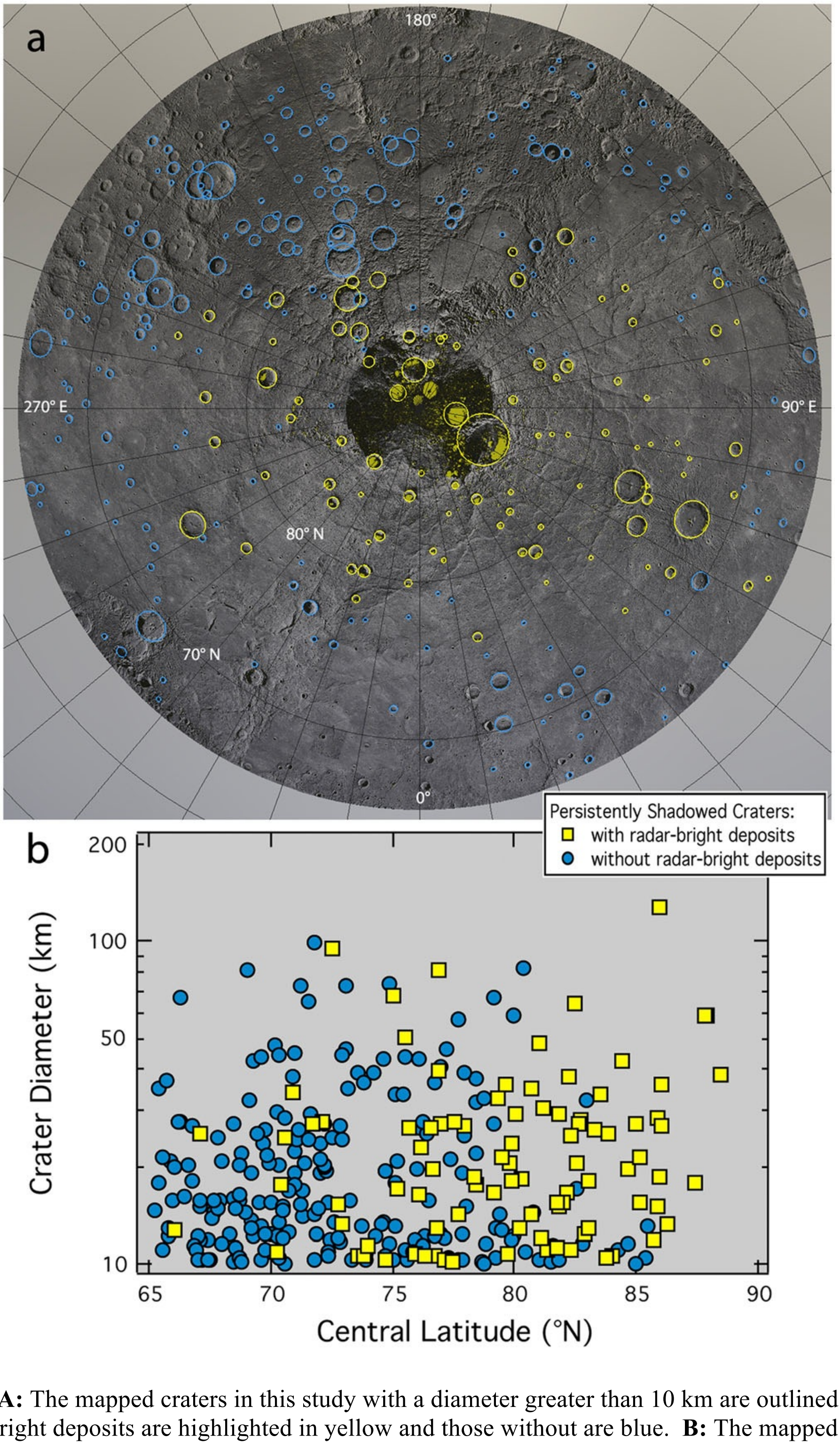

Figure 10. A: The mapped craters in this study with a diameter greater than 10 km are outlined. Those with radar-bright deposits are highlighted in yellow and those without are blue. **B:** The mapped craters are plotted as a function of their diameter and central latitude. Generally, as latitude increases towards the pole, craters are more likely to host radar-bright deposits (Chabot et al., 2012).

Nearly all of the persistently shadowed craters within 10º of the North Pole also host radar-bright material. Those persistently shadowed craters within 10º of the pole that did not host radar-bright material were primarily craters with diameters less than 20 km. South of 80º N, persistently shadowed craters hosting radar-bright deposits are not evenly distributed. Radar-bright deposits are distributed more heavily near 90º E longitude and less so around 270º E (Chabot et al, 2012). These areas are referred to as "cold poles." Solar insolation is significantly less at these areas because of the planet's highly eccentric orbit, resulting in temperatures up to 130 K less than the corresponding "hot poles" at 0º E and 180º E (Vasavada et al., 1999). This spatial distribution supports the suggestion that the lower-latitude cold poles provide a more stable thermal environment for hosting water ice than hot poles (Harmon et al., 2001, Harmon, 2007, Harmon et al., 2011).

During previous studies, however, image coverage, and consequently the mapping of shadow, was incomplete near Mercury's North Pole. My research addresses the data gap by completing a north polar mosaic of Mercury and mapping regions of persistent shadow. Mercury's south polar region was repeatedly imaged during one of the early MDIS campaigns as part of the mission's science phase. Because of MESSENGER's highly eccentric orbit, an analogous campaign of regularly repeated images for the North Pole could not be complete. The spacecraft has a maximum altitude of nearly 15,200 km in the south and a minimum altitude between 200 and 500 km in the north. Thus when MESSENGER is orbiting the North Pole, there is a significantly smaller image footprint, impacting the balancing of imaging and data volume constrains of not only MDIS, but also of other instruments contending for low-altitude measurements. The global imaging campaigns completed by MDIS during the primary mission did, however, provide a myriad of surficial views of Mercury's north polar region. Now that MDIS has imaged 100% of the planet, a qualitative and quantitative analysis of the spatial distribution of persistently shadowed areas from Mercury's cratered North Pole with radar-bright deposits can be completed.

Geologic Setting

Along with the other planets of the Solar System, Mercury formed about 4.6 Ga as rotating clouds of gas and dust contracted and flattened to form a thin disk in a plane around the sun. Mercury formed as rocky planet material clumped together in the protostellar cloud. This innermost planet is composed of a dense iron-rich core, encapsulated by a rocky mantle, rich in magnesium and iron silicates. Early differentiation and later volcanic and magmatic activity led to the separation of minerals with lower melting points in the crust and those with higher melting points in the underlying mantle. One of Mercury's unique features is its high density, which implies greater than 60% of the planet is a metal-rich core (Cameron et al., 1988).

Much of the planet is cratered and ancient. Less cratered plains, often volcanic in origin, scatter the surface. These plains are younger than the heavily cratered materials, as indicated by superposition (Pike, 1988). MESSENGER flyby imagery indicates that Mercury was volcanically active during the first half of its geologic history; this activity included both explosive and effusive activity. The surface is also riddled with many scarps produced by tectonic forces. These long, rounded, lobate cliffs are thought to have formed as a result of the entire planet cooling and contracting (Thomas et al., 1982).

Measurements of Mercury's gravity field have been collected to understand the planet's internal mass distribution, which impacts thermal and tectonic evolution. Because of MESSENGER's highly elliptical orbit, the northern hemisphere has been mapped for regional gravitation structures at an initial periapsis altitude of 200 km, but the southern latitudes have been limited to measurements at long wavelengths. Smith et al. (2012) combined gravitational measurements from Radio Science and topography measurements from the Mercury Laser Altimeter to produce a map of crustal thickness of Mercury's northern hemisphere (Fig. 11). The map indicates that the crust is on average thickest near the equator at 50 to 80 km and thins toward the north polar region, where the crust averages between 20 to 40 km. The thinnest crust is present below the northern lowlands (Zuber et al., 2012). The Caloris basin overlies locally thin crust, which is consistent with the interpretation that crustal thinning beneath basins contributes to gravity anomalies, as observed at the mass concentration basins on the Moon (Neumann et al., 1996) and Mars (Zuber et al., 2000).

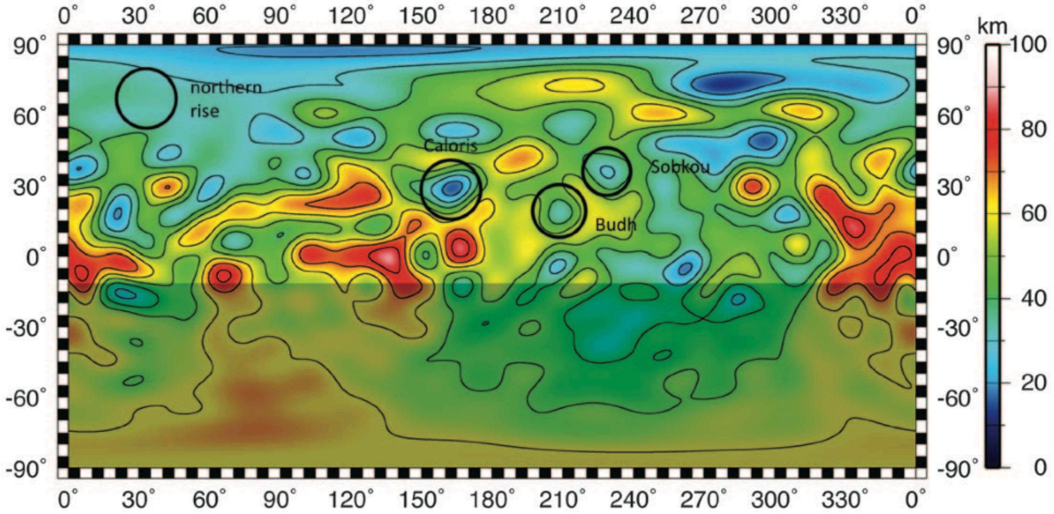

Figure 11. The crustal thickness is displayed using cylindrical projections. The northern rise, Caloris Basin, Sobkou, and Budh are labeled for reference (Smith et al., 2012).

MESSENGER's X-Ray Spectrometer (XRS) has yielded surface compositional measurements that indicate the planet's crust is intermediate between basaltic and more ultramafic compositions (Nittler et al., 2011). Melting experiments with candidate mantle compositions have shown consistency with the XRS measurements (Charlier et al., 2012). Using XRS and melting experiments' results, a density contrast between the crust and mantle is estimated to be 200 kg m^{-3} (Smith et al., 2012). A mean crustal thickness of 50 km is estimated (Smith et al., 2012) based on gravitational flyby observations (Smith et al., 2010), topography measurements (Zuber et al., 2008), and constraints from tectonic models for the depth extent of faulting (Nimmo, and Watters, 2004).

The rotational axis of Mercury is oriented nearly perpendicular to the planet's orbit, creating virtually no experienced tilt for the planet (Colombo and Shapiro, 1966). Thus the sun is almost always striking the polar surfaces at an extremely low angle. As a result, some of the interiors of the polar craters never experience sunlight. These regions are permanently shadowed, resulting in persistently cold temperatures (Chabot et al., 2013).

Mercury has no appreciable atmosphere, which also contributes to thermal stability when considering water ice. Mercury instead has a thin exosphere, composed primarily of oxygen, sodium, hydrogen, helium, and potassium. The exosphere is built from atoms blasted off the surface by micrometeoroid impacts and solar wind (Hunten et al., 1988). This tenuous atmosphere does not do an adequate job of trapping heat, regardless of the significant amount of intense heat striking the surface from the proximal sun. This lack of a true atmosphere contributes to allowing Mercury to host thermally stable environments for water ice (Rasool et al., 1966).

Mercury is particularly interesting to study as an end member example for other terrestrial, rocky planets. It is a unique environment with many extreme properties: the smallest diameter, the greatest density, the oldest surface, and the largest daily surface temperature variations. And yet, Mercury is the planet that has been least explored. Only two NASA missions have contributed to Mercury data: Mariner 10 launched in 1973 and

MESSENGER launched in 2004. Mariner 10 completed three flybys of the planet, imaging nearly 45% of the planet. It was not until July 2013 that 100% coverage of the planet was reached when MESSENGER was in orbit. Studying this end member is an important step in better understanding planet formation and evolution of the rest of this Solar System.

Methods

Imaging Details

The Mercury Dual Imaging System (MDIS) has two cameras: a wide-angle camera (WAC) and a narrow-angle camera (NAC). Both cameras are based on charge-coupled devices and take images of Mercury in visible and near-infrared light. The multi-spectral MDIS maps the landforms and spectral variations on Mercury's surface in monochrome, color and stereo. The cameras are gimbaled, allowing images to be captured from a wide area without requiring the spacecraft to remaneuver itself. When light enters the MDIS through a 12 cm by 12 cm window, it is filtered so that only light of visible and near-infrared wavelengths pass. The light then enters either the WAC or NAC. Only one camera is operated at a single point in time due to temperature constraints placed on the system.

The WAC has a 10.5° by 10.5° field of view and can image Mercury through monochrome and 11 additional color filters across a 395 to 1,040 nm wavelength range, allowing the planet to be viewed in visible through near-infrared light. Light in different wavelengths combine to produce color images. Multi-spectral imaging is used to distinguish rock types on the planet's surface. The NAC has a 1.5° by 1.5° field of view can take black-and-white images at high resolution with its single visible light filter, allowing for more detailed analyses of the surface.

The spacecraft's orbit is highly eccentric, with its lowest point above the surface about 200 km and its highest point greater than 15,000 km. The periapsis is over Mercury's north polar region, thus the first attempts to image in permanently shadowed regions were made in this area. NAC images do not provide any details of shadowed surfaces of this region because of image smear. Smear is caused by the spacecraft's motion during the long exposure time required to produce a signal above the background level. The WAC broadband filter images with exposures of 10 ms are used to study surface details of permanently shadowed areas. The broadband clear filter has a central wavelength of 700 nm and a bandwidth 600 nm.

Individual Crater Analysis

When looking at craters on an individual basis, images were gathered from the MESSENGER Mercury Dual Imaging System (MDIS) Image Search from the data collections in the Science Operations Center Archives. Wide-angle camera (WAC) images that were of observation type polar dark craters and had an exposure time between 40 and 80 milliseconds were targeted. The exposure time parameters reflect the length of time the camera's shutter is open when taking an image, proportional to the amount of light that reaches the image sensor.

Images of individual craters returned from this search, were downloaded and processed using Integrated Software for Imagers and Spectrometers (ISIS), designed to manipulate imagery collected by planetary missions. The images were downloaded as MESSENGER/MDIS Experimental Data Record (EDR) products and converted into ISIS cubes. Next, locations of latitude and longitude were computed for each image by running SPICE kernels. The images were then corrected for impurities during calibration using mdiscal. The cubes were next trimmed to remove null pixels using the trim command. Finally, they were re-projected into the polar stereographic projection and mapped to the same window extent of latitude and longitude.

These craters were then opened in qview, a program used to display cubes for an interactive analysis. Using the grayscale tool, the inside of the crater was targeted in order to stretch the image to bring out the color differentiations within the crater itself, determining areas hosting intriguing dark material. Once the crater interior was stretched enough to emphasize reflectivity and topographic differences on the floor, the image was converted from a cube to a standard JPEG format using isis2std. In this export, a manual stretch was implemented, setting the minimum and maximum pixel values to the corresponding extremes that created the appropriate stretch in qview.

Craters that showed reflectivity-dark material in the stretched image were investigated further. For each of these craters, images were downloaded from the data collections in the Science Operations Center Archives that showed as many views of the crater in different lighting conditions as possible in order to help map an area of persistent shadow. The images were imported as MESSENGER/MDIS EDR products and converted into ISIS cubes using ISIS command mdis2isis. Next, SPICE kernels were determined for each camera cube using spiceinit in order to compute ground positions and photometric viewing angles. The images were then corrected for dark current, linearity, smear, uniformity, and absolute coefficient during calibration using mdiscal. Finally, the edges of the input cubes were trimmed to eliminate null edge pixels using the trim command. Each trimmed cube was then manually projected into a polar stereographic projection using cam2map. The cubes were then modified to show the same latitude and longitude window using the image that had the most extensive view of the target crater as the map using map2map. Finally, the cubes were exported as JPEGs using the isis2std command for further analysis and shadow mapping.

Areas of persistent shadow within individual craters that had noticeable intriguing dark material were mapped in Adobe Photoshop. To begin, the JPEGs of all of the different lighting views were imported and duplicated. The duplicated layers were filtered and adjusted using the Threshold tool. This filter converted the image into high-contrast black-and-white images. The Threshold dialog box displays a histogram of the luminance levels of the images pixels. The slider below the histogram was dragged until the threshold level distinctly separated the areas of shadow from non-shadow for each individual picture. In order to find this exact level, the original image was turned on below the duplicate layer. The duplicate layer was then placed on a mid-range transparency level so that the original could be seen below. Thus as the duplicate was reclassified, it was made certain that the lines between shadow and non-shadow matched on top of the original image. This distinct threshold tended to remain around the first divot displayed in each image's histogram. The final product was a separate layer for each lighting view that had been reclassified into two categories: black shadow and white non-shadow. The duplicated images were then inverted so that shadowed areas were represented by white. All of the inverted threshold products were duplicated and merged. The area that was shadowed in every lighting view appears pure white. A white gradient tends from this pure color to a lighter white, representing regions that are shadowed in some lighting views, but not all. The Magic Wand tool was used to select the pixels of the pure white, persistently shadowed area by color and tone. This area was then extracted and added as its own layer.

The stretched polar dark crater image that was initially investigated was imported to Photoshop and cropped to show only the interior of the crater. Arecibo radar and MLA reflectivity data were then overlain on each targeted crater to investigate the relationships between the dark material, mapped shadow, and these two variables. Radar and reflectivity cubes were similarly re-projected into the north polar stereographic projection and the latitude and longitude window of the base map image using the map2map command in ISIS. Each targeted crater could then be observed based on four main layers: a stretched image emphasizing intriguing dark material, a mapped region of persistent shadow, Arecibo data indicating radar-bright material having the same radar signature as pure water ice, and reflectivity data comparing the dark material to average surface reflectivity measurements. In the reflectivity dataset, blue spots represent MLA dark areas at a single wavelength of 1064 nm.

Areas of persistent shadow, radar-bright material, and dark deposits were quantitatively correlated. Each crater with a diameter of 5 km or greater was marked with Boolean values with respect to these three categories. “True” values were assigned in each respective category when a crater showed regions of shadow, radar-bright material, or dark deposits. “False” values were given in a category when the crater did not have the respective quality of shadow, radar signature, or dark material. When there was no data for the crater, it was assigned “Null” values.

With these three categories, the relationship of these variables for the craters in the study area of 75º N and northward was quantified. Specifically, I calculated how often craters showed both persistent shadow and radar-bright material, showed no persistent shadow and no radar-bright material, showed persistent shadow and no radar-bright material, and showed no persistent shadow and radar-bright material by setting up simple count ratios for all craters showing dark material.

Regional Analysis

In order to map the region of 84º N and northward, images were processed in batch mode because of the large spatial extent under study. Images used in the regional analysis were WAC images from the 748.7 nm Filter G and 700 nm Filter B. They were converted into ISIS cubes using mdis2isis and calibrated using mdiscal. The cubes were then given location data via SPICE kernels using spiceinit. Instead of using the default predicting point kernels, a digital elevation map (DEM) was used to take the topography of the surface into account in order to produce better registration between the images. The batch was then trimmed to remove null pixels. In order to create a map for the north polar region, maptemplate was used, creating a map in the polar stereographic projection with a 200 m/pixel resolution with defined central coordinates at 90º N, 0º E, minimum coordinates at 84º N, 0º E, and maximum coordinates at 90º N, 360º E. Next, cam2map was used to map project each individual image by the specifications of the map template just created. Finally, a map of the pole using all the available images was created using automos with an average priority, which mosaicked the imagery and averaged all of the overlapping areas together.

This full mosaic of the study area was used to map areas of persistent shadow. Thresholding of the imagery was completed using the fx command, which reclassified the images' pixels into two values: 0 for sunlit terrain and 1 for shadowed. The images from MDIS Filter G were split into two groups before thresholding, determined by their central latitude. A pixel value of 0.005 was used as the threshold between sunlit and shadowed regions for images with central latitudes less than 85º N. A value of 0.0025 was used for images centered at or above 85º N. These threshold values were determined through trial and error runs of individual images. The central latitudes were recorded, as well as the pixel value that best separated the images into shadowed and non-shadowed parts. Images of higher latitude consistently needed lower pixel values when thresholding because these regions are receiving less sunlight thus the images are darker, requiring a smaller value to threshold the difference between shadow and non-shadow. The images from MDIS Filter B were thresholded using an fx value of 0.0025. The value that best separated the images into shadowed and non-shadowed terrain did not change with latitude for these images because they were all significantly dark.

After these groups of images were thresholded, a mask was run to preserve null pixels. These pixels are not covered in the image footprint, so it would be incorrect to classify them as either sunlit or shadowed when these areas were simply not imaged. Mosaics were created using automos to average all the thresholded images that are either 0 or 1 in value, thus preserving the pixels that are shadowed in all of the images with a value of 1. The mosaics of each group of images were then mosaicked together and pixels were saved only when they equaled 1 using the fx command. Mask was used again to add null pixels back in so shadowed areas were not confused with areas that had never been imaged. The mosaic was re-projected to the study area and finally, isis2std was used to export the shadow map into a standard format.

The areas of radar-bright material were formatted on top of the full mosaic map that shows regions of persistent shadow. The radar-bright material cube was reprojected into the polar stereographic projection using cam2map. The output was then mapped to the same window extent of latitude and longitude using the map template created for the mosaic. The differences in spatial distribution between persistent shadowed regions and radar-bright deposits were observed.

Results

Individual Crater Results

726 WAC images of observation type polar dark crater were analyzed for the presence of dark material. From these images, 46 craters were distinguished (Fig. 12). Initially, 30.4% of the craters were identified with definite dark material (Table 1). 28.3% of the polar dark craters showed signs of possible dark material (Table 2). The qualifier 'possible' is used because the images in this category were somewhat darkened with considerable saturation. This darkness makes it difficult to distinguish topographic features, shadows, and possible dark material from one another. An additional 28.3% of the distinguished craters lacked dark material (Table 3). Images of these craters were not of high enough quality where the surface floor could be seen. From the available views of these craters, no dark material was determined. Finally, 13.0% of the distinguished craters that were recognized from WAC images were too saturated, smeared, or dark to distinguish any surface characteristics (Table 4). For these craters, it is not possible to say whether dark material was present due to lack of image quality.

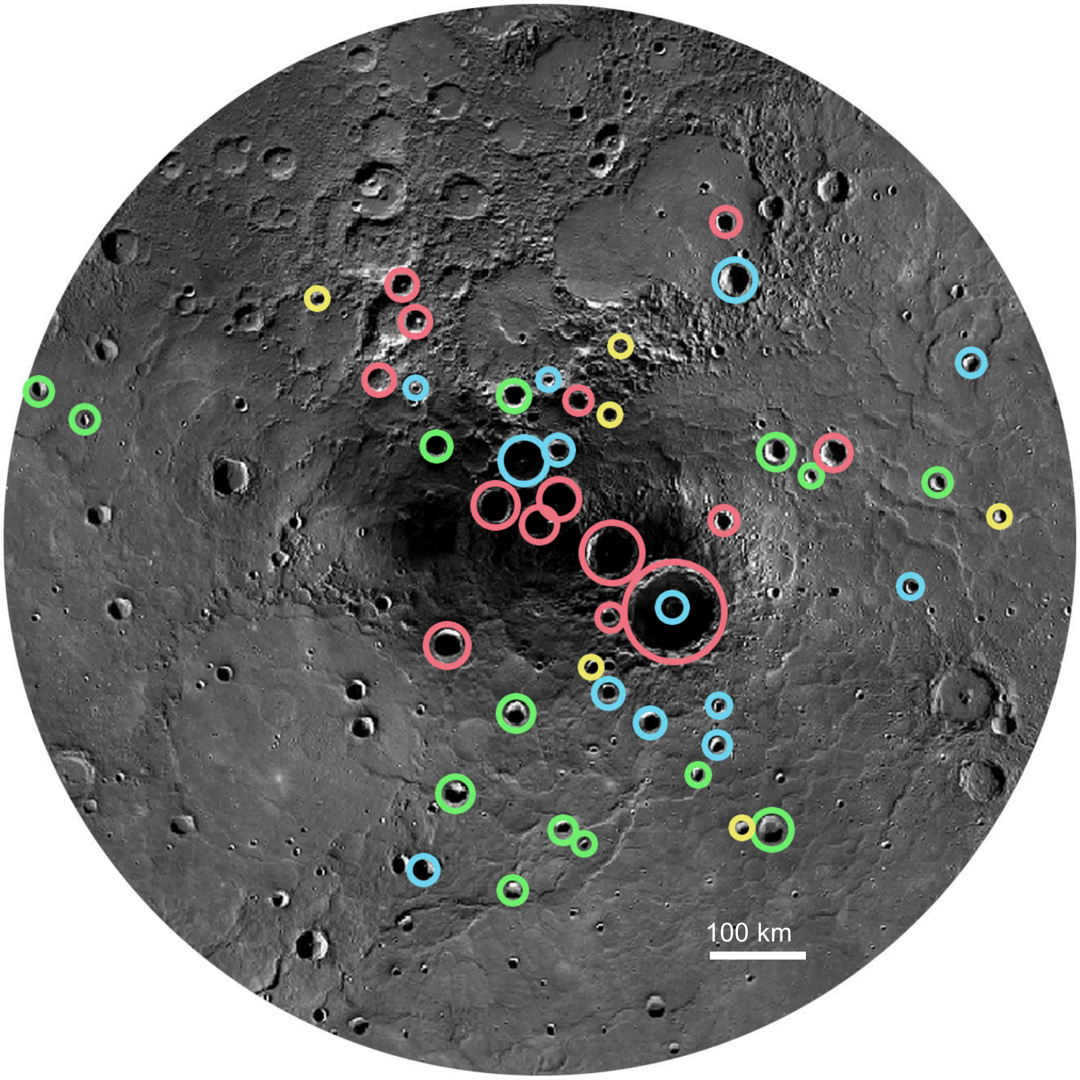

Figure 12. Each crater that was analyzed individually is circled. Craters outlined in green revealed definite dark material, craters outlined in blue showed possible dark material, craters outlined in red did not show evidence of dark material, and those outlined in yellow are inconclusive due to lack of high-quality imagery.

Craters identified with definite dark material ranged from 12 to 31 km in crater diameter and 75° to 86° N in central latitudes (Table 1). Craters that lacked dark material ranged from 9 to 60 km in crater diameter and 79.5° to 89° N in central latitudes (Table 3). Craters lacking dark material spanned a greater crater diameter range and were present in higher latitudes than those hosting dark material (Fig. 13).

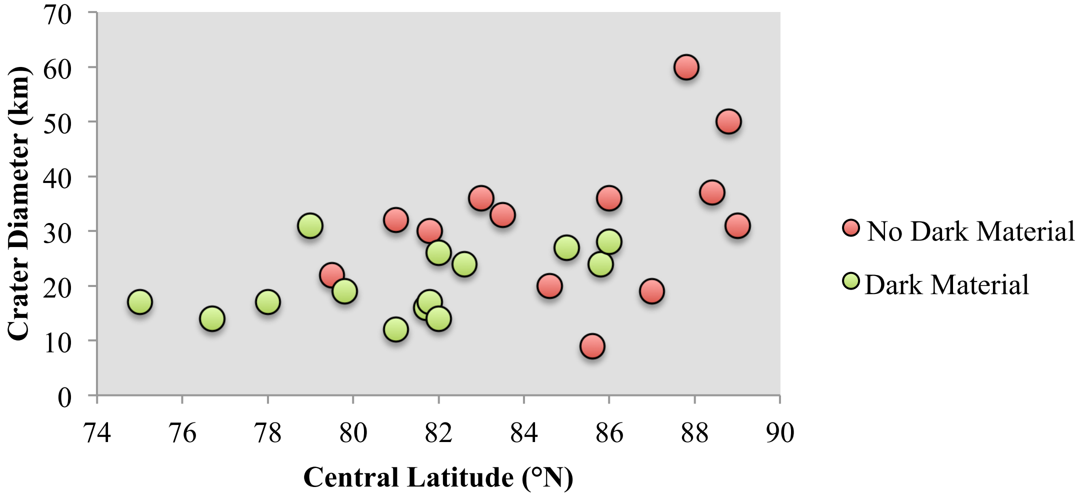

Figure 13. Individually investigated craters that had no dark material and definite dark material are plotted as a function of their diameter and central latitude. Generally, as latitude increases towards the pole, the presence of revealed reflectivity-dark deposits decreased.

For craters that showed definite dark material, radar-bright material never fell outside the bounds of reflectivity-dark material. Radar-bright deposits showed a strong correlation to dark material revealed from stretched WAC images, even aligning well with the irregular perimeters of the intriguing dark deposits. For craters Unnamed A, Unnamed B, Unnamed J, and Unnamed K, radar data was not strong enough and insignificant. Furthermore, craters showing reflectivity-dark deposits never had dark material or radar-bright signatures present beyond the extent of persistent shadows. Craters did, however, sometimes show reflectivity-dark and radar-bright deposits smaller than the reach of persistent shadows. This size difference could be because such material does actually take less area than its hosting crater's region of persistent shadow, or it could be due to MESSENGER not having images of the crater in all existing sunlight conditions, causing a mapped region of persistent shadow to cover more area than the region's persistently shadowed area.

The craters that showed possible dark material were further analyzed for spatial relationships between the possible dark material, radar data, and areas of persistent shadow. Radar data spatially correlated with 84.6% of these craters. The 15.4% lacking spatially correlated data had no significant radar data for their locale, as opposed to showing strong radar data that did not align with possible dark material. After further analyzing the possible dark material, the craters identified in the sample population were re-classified as hosting dark material (53.2%), as hosting light material (4.2%), as not revealing dark or light material (29.8%), or as not having enough quality images to make a determination (12.8%) (Fig. 14).

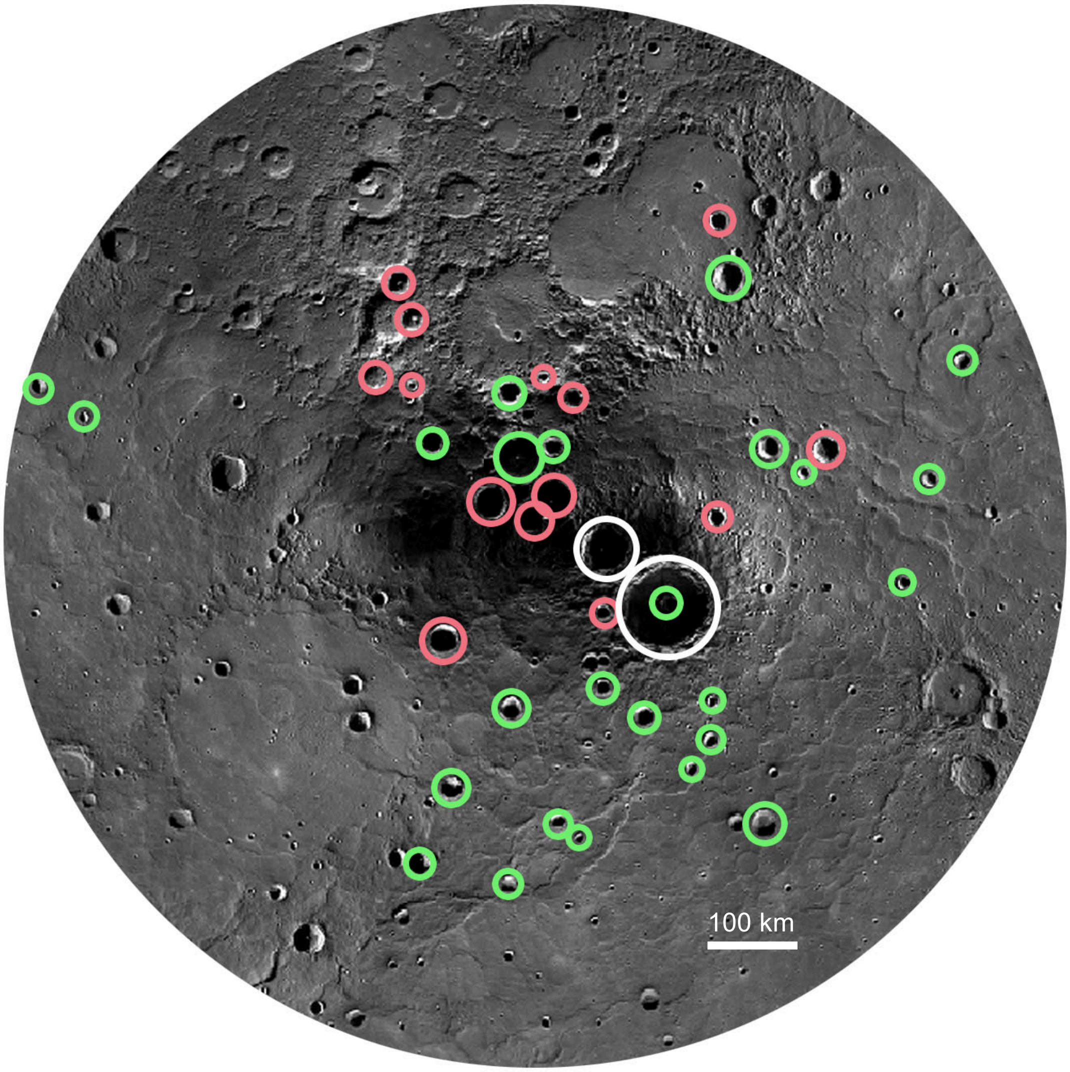

Figure 14. Each crater that was analyzed individually is circled. After further analyzing the "possibly dark craters," craters outlined in green were determined to host definite dark material, craters outlined in red did not show evidence of dark material, and those outlined in white showed reflectivity-light material.

With the re-classification, craters identified with definite dark material ranged from 12 to 54 km in crater diameter and 75° to 87° N in central latitudes (Table 5). Craters that lacked dark material ranged from 8.5 to 60 km in crater diameter and 79.5° to 89° N in central latitudes (Table 6). Craters lacking dark material were generally still present in latitudes higher than those of craters hosting dark material (Fig. 13).

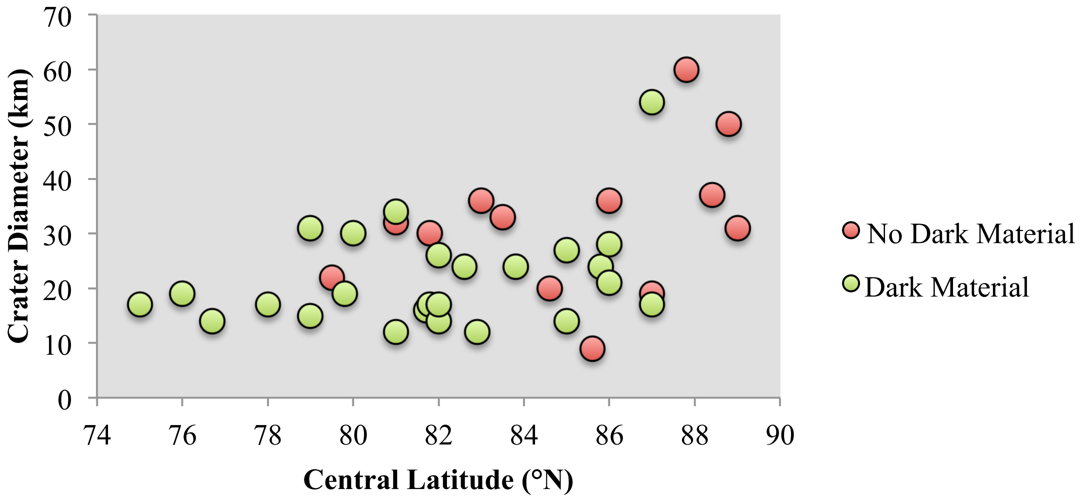

Figure 15. Individually investigated craters that had no dark material and definite dark material are plotted as a function of their diameter and central latitude. Generally, as latitude increases towards the pole, the presence of revealed reflectivity-dark deposits decreased.

Finally, two craters revealed possible reflectivity-light deposits in stretched WAC imagery: Prokofiev and Kandinsky (Table 7). Their light material aligned with both radar-bright data and regions of persistent shadow.

Unnamed A Crater. This 17 km crater lies at 75° N, 253° E. A stretched WAC image of this crater shows a prominent reflectivity-dark spot on the northern floor (Fig. 16a). An area of mapped shadow shows that the dark material lays within the bounds of the area of persistent shadow in the crater (Fig. 16b). There is no radar data for this region.

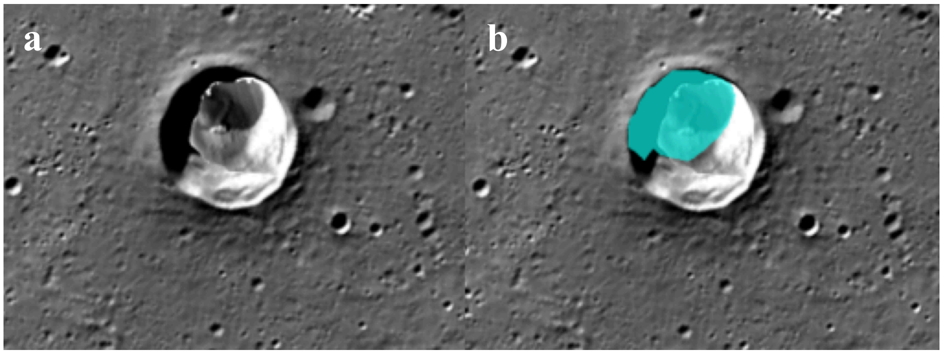

Figure 16. MDIS WAC image of Unnamed A crater (17 km diameter) with: (**a**) a stretched WAC broad-band-filter, 40-ms-exposure image overlain, showing the reflectivity-dark deposit within the crater; (**b**) both a mapped persistent shadow (turquoise) and the stretched WAC image overlain. There is no radar data for this crater.

Unnamed B Crater. This crater has a 14 km diameter and is positioned at 76.7° N, 255° E. Although streaky, a stretched WAC image of this crater reveals reflectivity-dark material in the central region of the crater, tending southeast (Fig. 17a). MESSENGER has not relayed WAC images revealing the entirety of this dark deposit. The mapped area of persistent shadow superimposed on top of the dark material shows that the dark material lies within the bounds of the persistently shadowed region (Fig. 17b). There is currently no radar data for this crater.

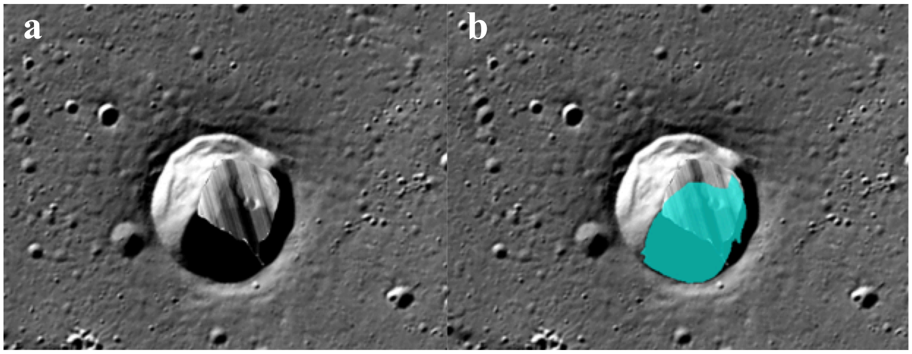

Figure 17. MDIS WAC image of Unnamed B crater (14 km diameter) with: (**a**) a stretched WAC broad-band-filter, 40-ms-exposure image overlain, showing the reflectivity-dark deposit within the crater; (**b**) both a mapped persistent shadow (turquoise) and the stretched WAC image overlain. There is no radar data for this crater.

Unnamed C Crater. This 17 km crater lies at 78° N, 97° E. A stretched WAC image shows a reflectivity-dark deposit in the southern half of the crater's interior (Fig. 18a). There is a strong spatial correlation between this dark material and a radar-bright deposit (Fig. 18b). The radar-bright deposit lies directly within the reflectivity-dark feature. The dark material also spatially correlates with the region of persistent shadow in this crater (Fig. 18c). It is completely contained by the boundaries of the shadowed region.

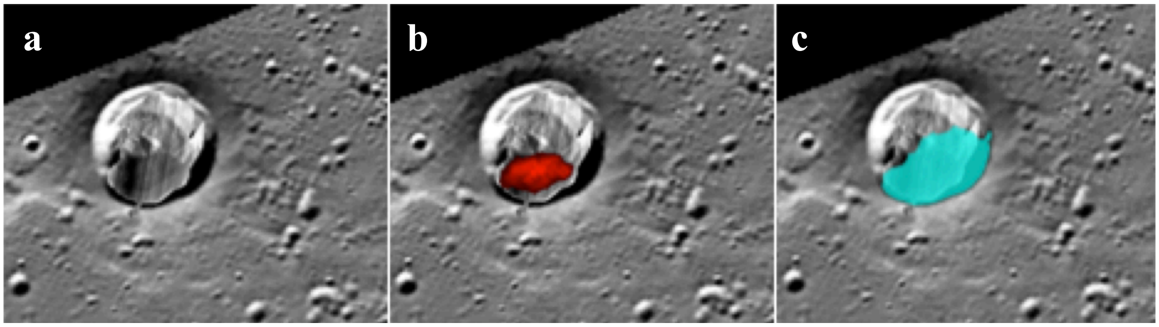

Figure 18. MDIS WAC image of Unnamed C crater (17 km diameter) with: (**a**) a stretched WAC broad-band-filter, 40-ms-exposure image overlain, showing the reflectivity-dark deposit within the crater; (**b**) both Arecibo radar (red) and the stretched WAC image overlain; (**c**) both a mapped persistent shadow (turquoise) and the stretched WAC image overlain. Arecibo radar was obtained with a range resolution of 1.5 km.

Berlioz Crater. Berlioz is a 31 km crater located on Mercury's north polar region at 79.3° N, 321° E. It hosts a substantial radar-bright deposit. Thermal studies have indicated temperatures in the crater's interior are on average between 50 and 100 K along the southeast region (Paige et al., 2013). A WAC image of the Berlioz crater was stretched to reveal a reflectivity-dark deposit on its crater floor (Fig. 19a). When radar data is overlain, a direct comparison shows an undeniable correlation between the spatial distribution of a radar-bright deposit and the crater's reflectivity-dark material (Fig. 19b). The area of persistent shadow within the crater also shows a strong correlation with these two variables (Fig. 19c). The shadowed region hosts lower temperatures than the remainder of the crater and thus provides a more stable environment for persistent water ice. Berlioz is one of the best examples of a persistently shadowed crater hosting a radar-bright, dark material deposit to date.

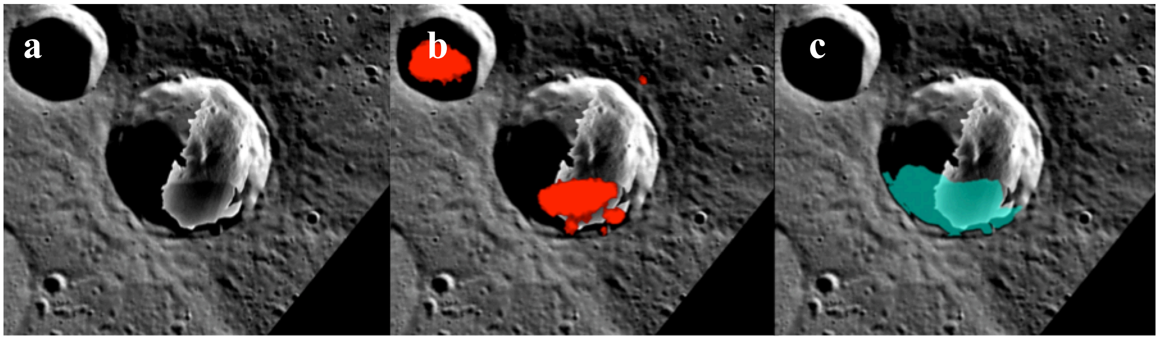

Figure 19. MDIS WAC image of Berlioz crater (31 km diameter) with: (**a**) a stretched WAC broad-band-filter, 40-ms-exposure image overlain, showing the reflectivity-dark deposit within the crater; (**b**) both Arecibo radar (red) and the stretched WAC image overlain; (**c**) both a mapped persistent shadow (turquoise) and the stretched WAC image overlain. Arecibo radar was obtained with a range resolution of 1.5 km.

Unnamed D Crater. This crater has a diameter of 19 km and is located at 79.8° N, 356° E. A stretched WAC image reveals a significant reflectivity-dark deposit on the crater's floor (Fig. 20a). The radar data for this crater reveals a small radar-bright deposit that overlies part of the dark material (Fig. 20b). A mapped shadow on the crater floor lines up well with the crater's dark deposit (Fig. 20c). There is a point above the mapped shadow that appears to be reflectivity-dark but does not fall under the area of persistent shadow. This dark point is not part of the reflectivity-dark deposit, but is rather a topographical shadow.

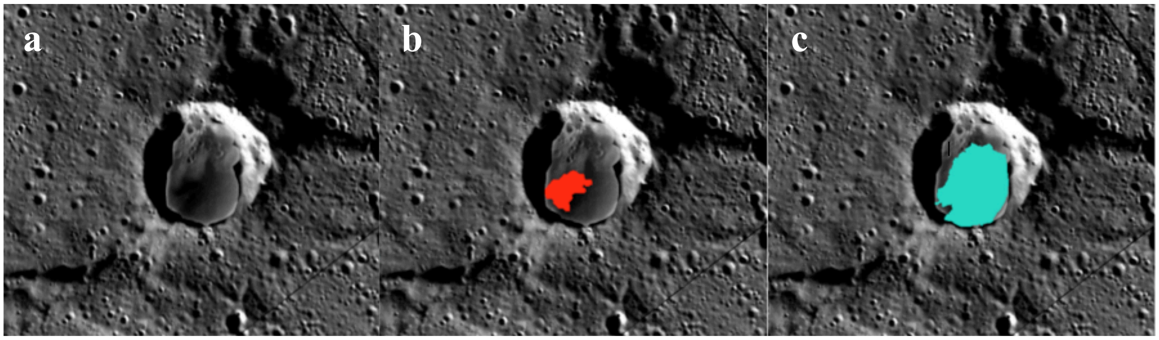

Figure 20. MDIS WAC image of Unnamed D crater (19 km diameter) with: (**a**) a stretched WAC broad-band-filter, 40-ms-exposure image overlain, showing the reflectivity-dark deposit within the crater; (**b**) both Arecibo radar (red) and the stretched WAC image overlain; (**c**) both a mapped persistent shadow (turquoise) and the stretched WAC image overlain. Arecibo radar was obtained with a range resolution of 1.5 km.

Unnamed E Crater. This 12 km crater lies at 81° N, 9° E. This crater hosts a considerable dark deposit that covers the majority of its floor (Fig. 21a). Arecibo radar data yields a radar-bright deposit that aligns itself with the northern edges of the crater's dark deposit (Fig. 21b). The mapped shadow of this crater shows strong spatial coordination with both the reflectivity-dark material and radar-bright deposit of Unnamed E crater (Fig. 21c).

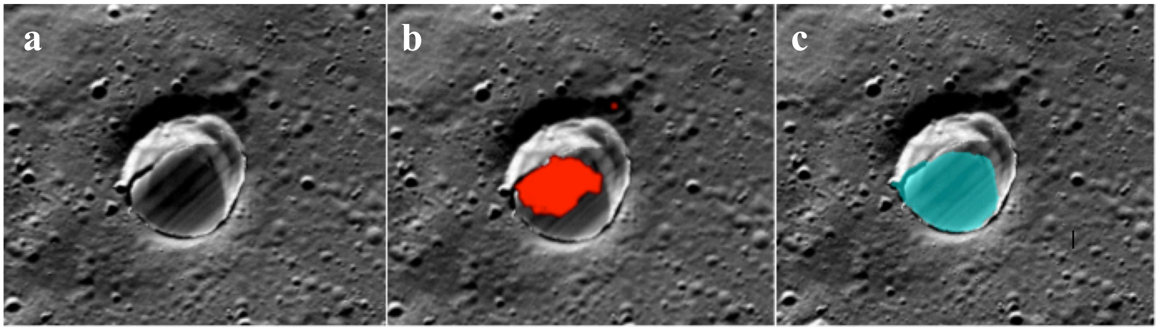

Figure 21. MDIS WAC image of Unnamed E crater (12 km diameter) with: (**a**) a stretched WAC broad-band-filter, 40-ms-exposure image overlain, showing the reflectivity-dark deposit within the crater; (**b**) both Arecibo radar (red) and the stretched WAC image overlain; (**c**) both a mapped persistent shadow (turquoise) and the stretched WAC image overlain. Arecibo radar was obtained with a range resolution of 1.5 km.

Unnamed F Crater. This crater has a diameter of 16 km and is centered at 81.7° N, 5° E. It hosts a reflectivity-dark material (Fig. 22a). Radar data shows a radar-bright deposit that aligns with the dark deposit's perimeter (Fig. 22b). The area of mapped shadow covers the areas of dark material and radar-bright data (Fig. 22c). The dark area between the two humps of persistent shadow is not a dark deposit, but is a shadow due to the crater's interior topography.

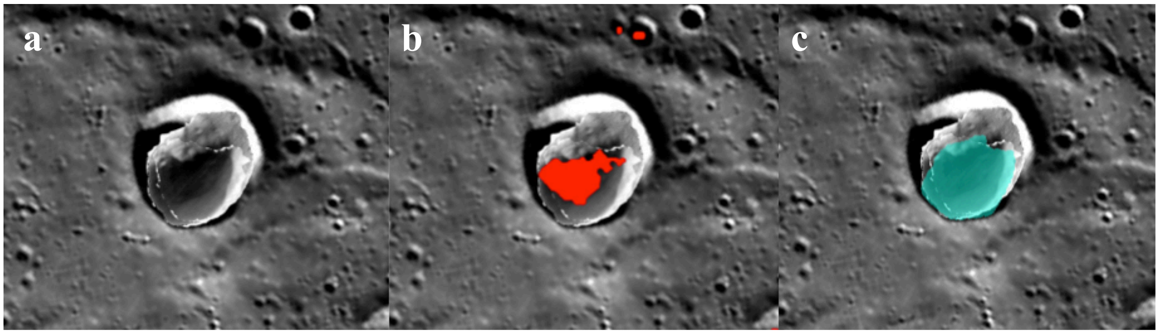

Figure 22. MDIS WAC image of Unnamed F crater (16 km diameter) with: (**a**) a stretched WAC broad-band-filter, 40-ms-exposure image overlain, showing the reflectivity-dark deposit within the crater; (**b**) both Arecibo radar (red) and the stretched WAC image overlain; (**c**) both a mapped persistent shadow (turquoise) and the stretched WAC image overlain. Arecibo radar was obtained with a range resolution of 1.5 km.

Unnamed G Crater. This 17 km crater is centered at 81.8° N, 34° E. An intriguing reflectivity-dark deposit on the crater's floor is revealed from a stretched WAC image (Fig. 23a). A radar-bright deposit is strongly spatially correlated with this dark material (Fig. 23b). The mapped area of persistent shadow for Unnamed G crater fully envelopes both the reflectivity-dark and radar-bright features (Fig. 23c).

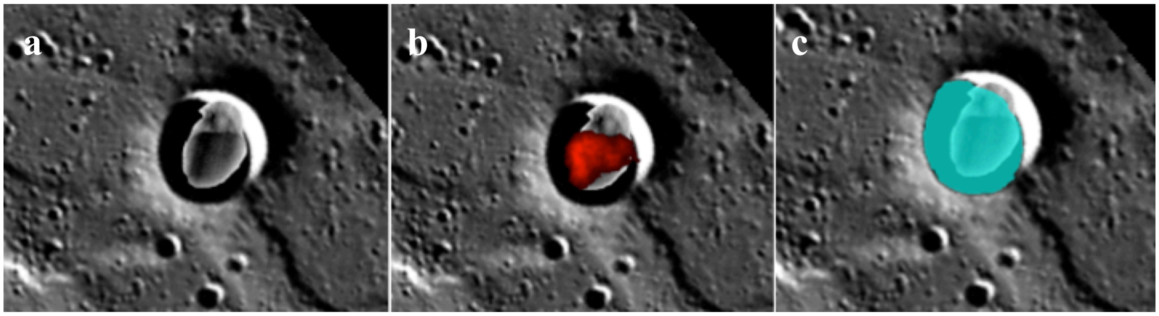

Figure 23. MDIS WAC image of Unnamed G crater (17 km diameter) with: (**a**) a stretched WAC broad-band-filter, 40-ms-exposure image overlain, showing the reflectivity-dark deposit within the crater; (**b**) both Arecibo radar (red) and the stretched WAC image overlain; (**c**) both a mapped persistent shadow (turquoise) and the stretched WAC image overlain. Arecibo radar was obtained with a range resolution of 1.5 km.

Unnamed H Crater. This crater has a 14 km diameter and is located at 82° N, 102° E. A stretched WAC image reveals a reflectivity-dark deposit within the crater's floor (Fig. 24a). Superimposing Arecibo radar data presents strong spatial correlation between this dark material and a radar-bright feature (Fig. 24b). Both the reflectivity-dark and radar-bright features are contained in the crater's area of persistent shadow (Fig. 24c).

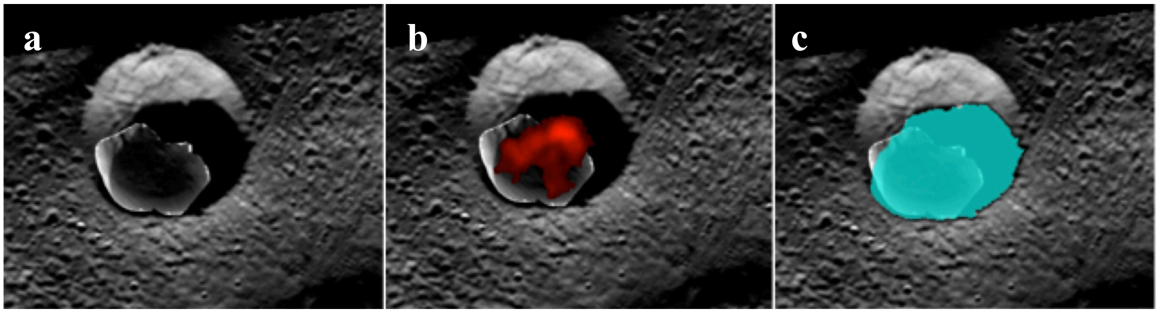

Figure 24. MDIS WAC image of Unnamed H crater (14 km diameter) with: (**a**) a stretched WAC broad-band-filter, 40-ms-exposure image overlain, showing the reflectivity-dark deposit within the crater; (**b**) both Arecibo radar (red) and the stretched WAC image overlain; (**c**) both a mapped persistent shadow (turquoise) and the stretched WAC image overlain. Arecibo radar was obtained with a range resolution of 1.5 km.

Ensor Crater. This 26 km crater lies at 82° N, 342° E. The crater's floor shows particularly intriguing reflectivity-dark features (Fig. 25a). The dark finger-like structures, however, are not dark deposits but rather shadows from topographical features. The radar data from this crater shows strong spatial correlation with the dark material (Fig. 25b). Finally, the area of mapped persistent shadow for Ensor encapsulates both the dark deposit and radar data of this crater (Fig. 25c).

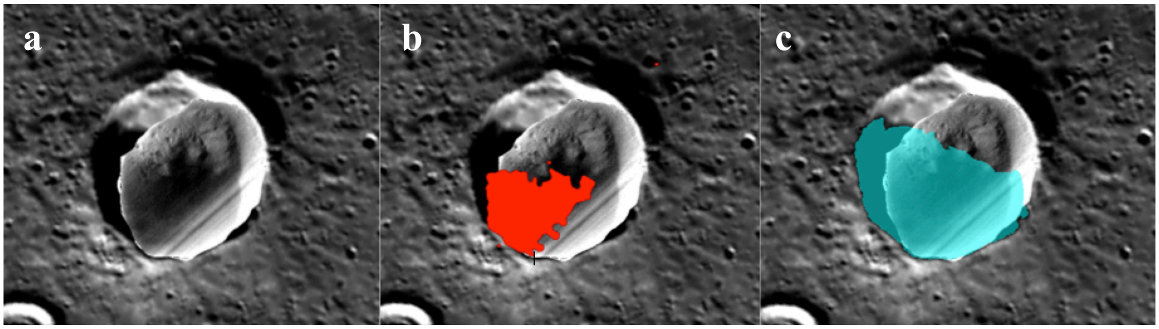

Figure 25. MDIS WAC image of Ensor crater (26 km diameter) with: (**a**) a stretched WAC broad-band-filter, 40-ms-exposure image overlain, showing the reflectivity-dark deposit within the crater; (**b**) both Arecibo radar (red) and the stretched WAC image overlain; (**c**) both a mapped persistent shadow (turquoise) and the stretched WAC image overlain. Arecibo radar was obtained with a range resolution of 1.5 km.

Unnamed I Crater. This crater has a diameter of 24 km and is centered at 82.6° N, 110° E. It hosts a sizable reflectivity-dark feature, as revealed by a stretched WAC image (Fig. 26a). Superimposed radar data shows a strong spatial correlation between this reflectivity-dark feature and a radar-bright feature (Fig. 26b). These two features lie within the boundaries of the mapped area of persistent shadow for this crater (Fig. 26c).

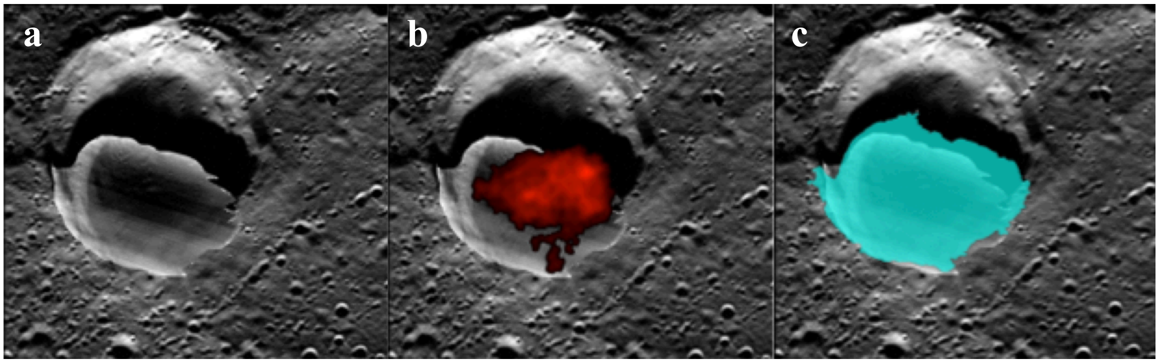

Figure 26. MDIS WAC image of Unnamed I crater (24 km diameter) with: (**a**) a stretched WAC broad-band-filter, 40-ms-exposure image overlain, showing the reflectivity-dark deposit within the crater; (**b**) both Arecibo radar (red) and the stretched WAC image overlain; (**c**) both a mapped persistent shadow (turquoise) and the stretched WAC image overlain. Arecibo radar was obtained with a range resolution of 1.5 km.

Remarque Crater. Remarque, a crater of 30 km diameter that lies at 85° N, 354° E, is another host of a sizable radar-bright feature (Fig. 27b). Thermal studies show consistent temperatures below 100 K (Paige et al., 2013). A reflectivity-dark deposit on the floor of this crater was revealed from a stretched WAC image (Fig. 27a). Again, overlain radar data and a mapped persistent shadow show strong spatial correlation with the crater's reflectivity-dark anomaly (Fig. 27b, c).

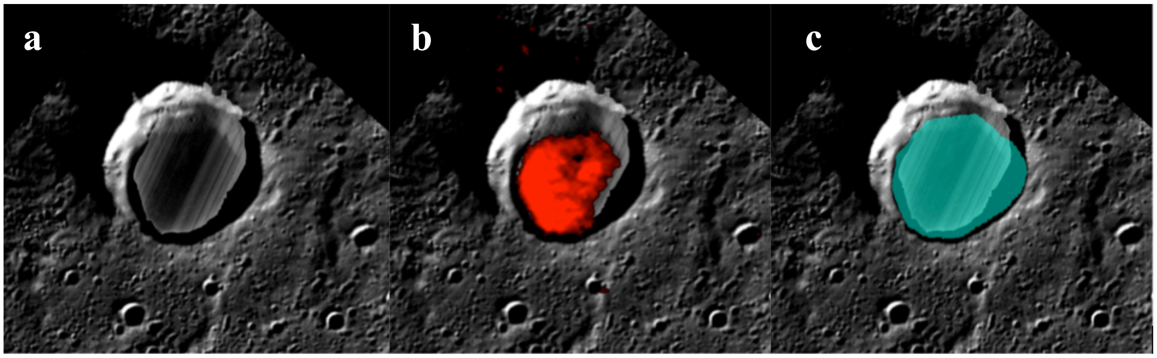

Figure 27. MDIS WAC image of Remarque crater (27 km diameter) with: (**a**) a stretched WAC broad-band-filter, 40-ms-exposure image overlain, showing the reflectivity-dark deposit within the crater; (**b**) both Arecibo radar (red) and the stretched WAC image overlain; (**c**) both a mapped persistent shadow (turquoise) and the stretched WAC image overlain. Arecibo radar was obtained with a range resolution of 1.5 km.

Unnamed J Crater. This 24 km crater lies at 85.8° N, 188° E. A stretched WAC image reveals a sizeable deposit of reflectivity-dark material covering the majority of the crater's floor (Fig. 28a). Radar data is not strong in this area and only reveals insignificant radar scattering (Fig. 28b). The mapping of an area of persistent shadow for this crater overlies the dark material with a strong spatial correlation (Fig. 28c).

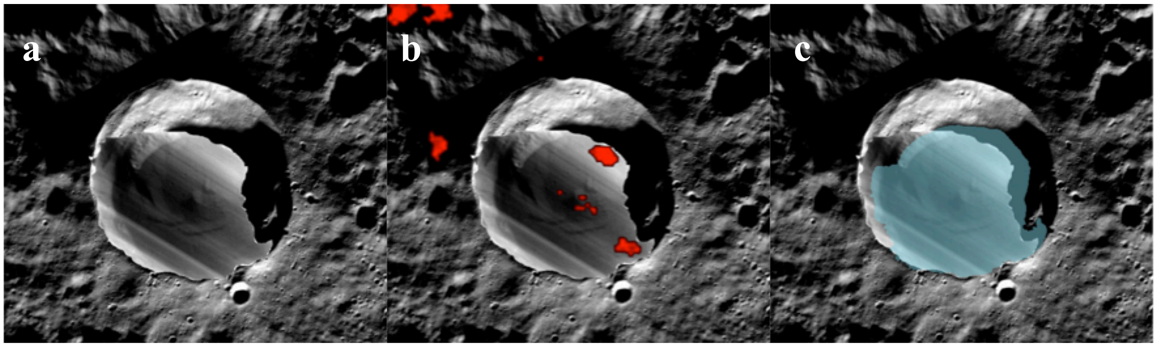

Figure 28. MDIS WAC image of Unnamed J crater (24 km diameter) with: (**a**) a stretched WAC broad-band-filter, 40-ms-exposure image overlain, showing the reflectivity-dark deposit within the crater; (**b**) both Arecibo radar (red) and the stretched WAC image overlain; (**c**) both a mapped persistent shadow (turquoise) and the stretched WAC image overlain. Arecibo radar was obtained with a range resolution of 1.5 km.

Unnamed K Crater. This crater lies at 86° N, 227° E and has a diameter of 28 km. It hosts significant reflectivity-dark material that contrasts the northern wall and floor (Fig. 29a). Again, radar data in this region is not strong and shows only insignificant radar scattering (Fig. 29b). The area of persistent shadow for Unnamed K crater shows very strong spatial coordination with the crater's dark material (Fig. 29c).

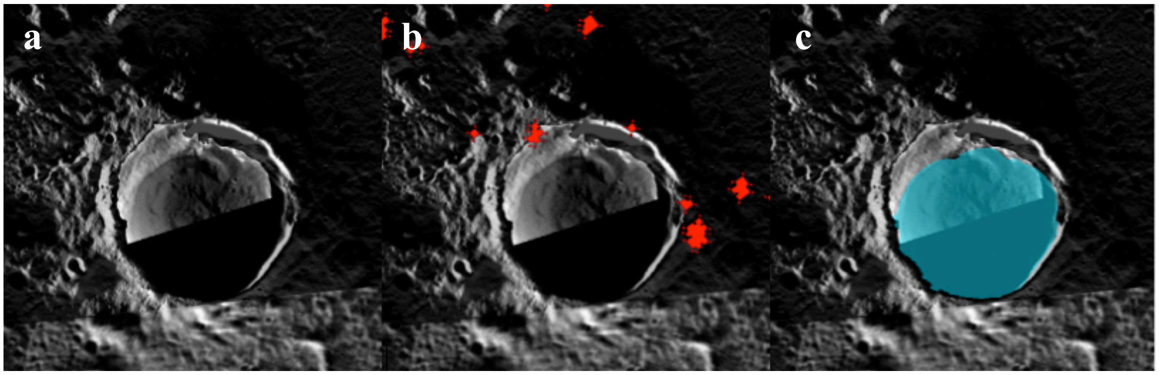

Figure 29. MDIS WAC image of Unnamed K crater (28 km diameter) with: (**a**) a stretched WAC broad-band-filter, 40-ms-exposure image overlain, showing the reflectivity-dark deposit within the crater; (**b**) both Arecibo radar (red) and the stretched WAC image overlain; (**c**) both a mapped persistent shadow (turquoise) and the stretched WAC image overlain. Arecibo radar was obtained with a range resolution of 1.5 km.

Unnamed L Crater. This crater of 19 km diameter, is positioned at 76° N, 112° E. A stretched WAC image reveals a sliver of the crater's interior, with an intriguing, incomplete, reflectivity-dark deposit (Fig. 30a). Radar data superimposed on top of the crater's interior matches up to the revealed perimeter of the dark material (Fig. 30b). A mapped area of persistent shadow encompasses both the reflectivity-dark and radar-bright deposit (Fig. 30c). The spatial correlation between these three variables indicates that this crater does indeed host a reflectivity-dark, radar-bright deposit in a region of persistent shadow.

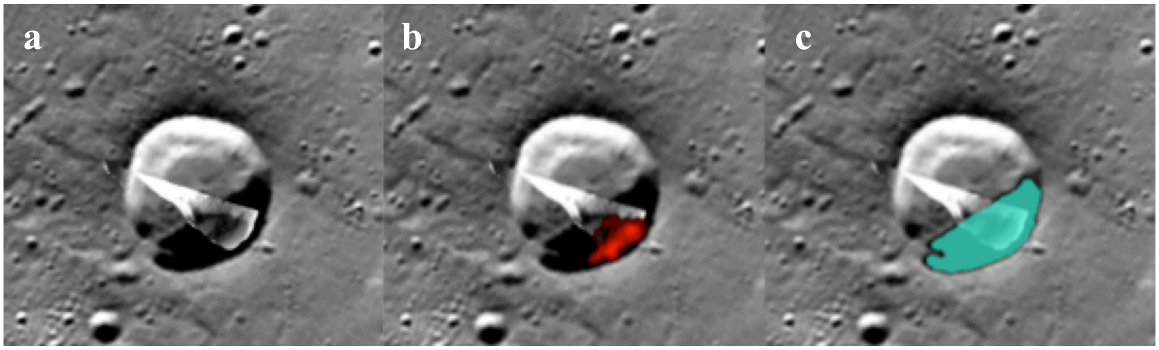

Figure 30. MDIS WAC image of Unnamed L crater (19 km diameter) with: (**a**) a stretched WAC broad-band-filter, 40-ms-exposure image overlain, showing the reflectivity-dark deposit within the crater; (**b**) both Arecibo radar (red) and the stretched WAC image overlain; (**c**) both a mapped persistent shadow (turquoise) and the stretched WAC image overlain. Arecibo radar was obtained with a range resolution of 1.5 km.

Unnamed M Crater. This crater is centered at 79° N, 82° E and has a diameter of 15 km. A stretched WAC image reveals an intriguing dark pattern in the center of the crater (Fig. 31a). The dark shape aligns with radar data and an area of mapped shadow (Fig. 31b; Fig. 31c). This spatial correlation suggests that the possible dark material identified in Unnamed M crater is in fact a radar-bright sublimation lag.

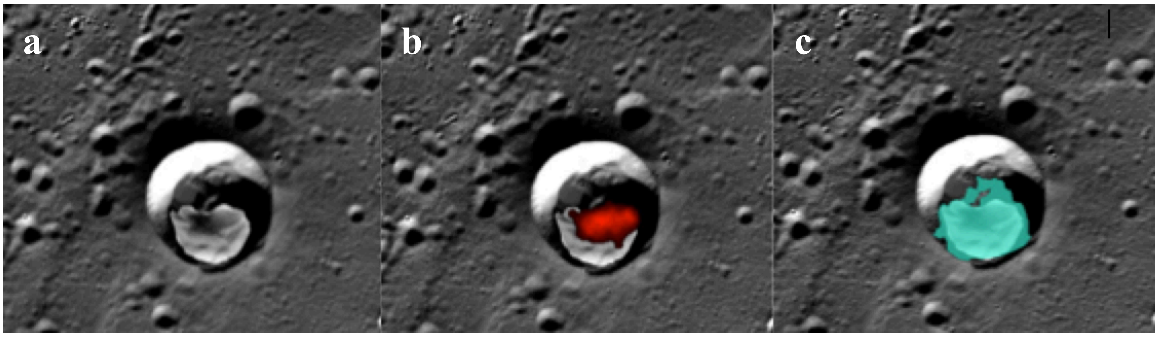

Figure 31. MDIS WAC image of Unnamed M crater (15 km diameter) with: (**a**) a stretched WAC broad-band-filter, 40-ms-exposure image overlain, showing the reflectivity-dark deposit within the crater; (**b**) both Arecibo radar (red) and the stretched WAC image overlain; (**c**) both a mapped persistent shadow (turquoise) and the stretched WAC image overlain. Arecibo radar was obtained with a range resolution of 1.5 km.

Varma Crater. This crater 30 km diameter is located at 80° N, 341° E. Varma's interior shows a reflectivity difference between the northern and southern halves of the crater (Fig. 32a). Arecibo radar data indicates radar-bright material that aligns with the reflectivity-dark border (Fig. 32b). Additionally, the mapped area of persistent shadow envelopes the dark deposit and radar-bright signature (Fig. 32c). The alignment of the possibly dark material, radar-bright signature, and persistent shadowing suggest that the reflectivity difference in Varma's stretched WAC image is indeed a dark deposit on the crater's floor.

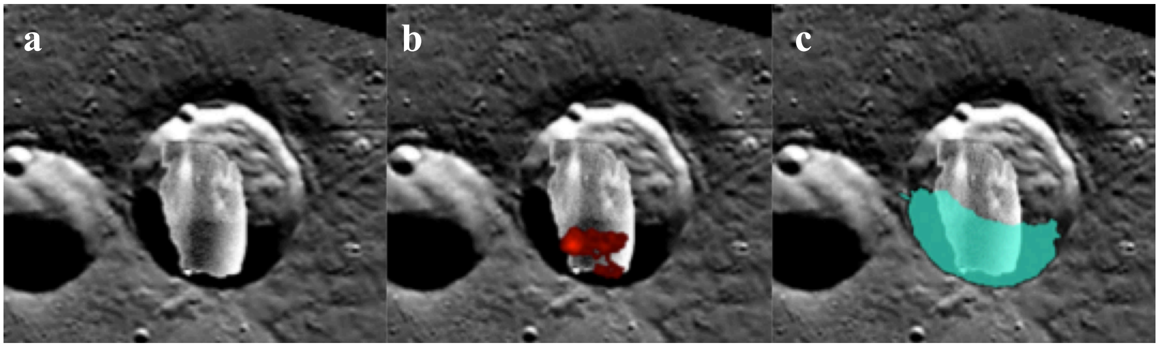

Figure 32. MDIS WAC image of Varma crater (30 km diameter) with: (**a**) a stretched WAC broad-band-filter, 40-ms-exposure image overlain, showing the reflectivity-dark deposit within the crater; (**b**) both Arecibo radar (red) and the stretched WAC image overlain; (**c**) both a mapped persistent shadow (turquoise) and the stretched WAC image overlain. Arecibo radar was obtained with a range resolution of 1.5 km.

Unnamed N Crater. This crater is positioned at 81° N, 142° E and has a diameter of 34 km. A stretched WAC image shows a possible dark deposit on its southern floor (Fig. 33a). Both radar data and Unnamed N's area of persistent shadow overlap with this dark material (Fig. 33b; Fig. 33c). This spatial correlation indicates that the reflectivity difference in the stretched WAC image of Unnamed N is showing a reflectivity-dark deposit.

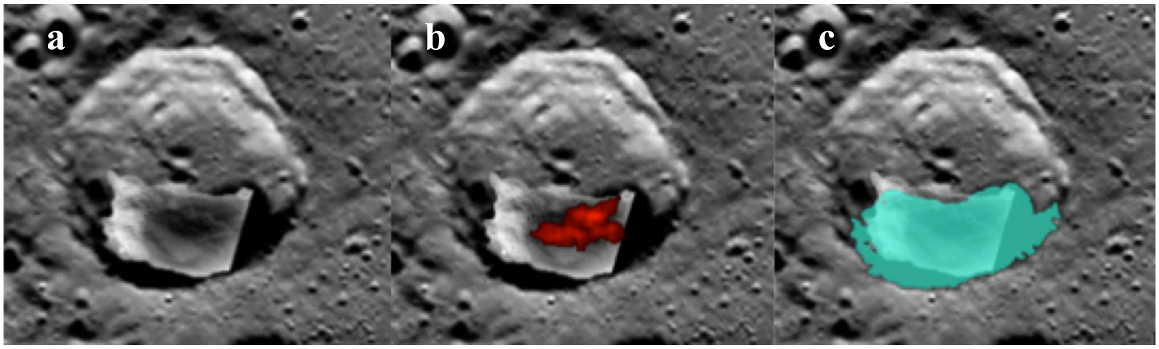

Figure 33. MDIS WAC image of Unnamed N crater (34 km diameter) with: (**a**) a stretched WAC broad-band-filter, 40-ms-exposure image overlain, showing the reflectivity-dark deposit within the crater; (**b**) both Arecibo radar (red) and the stretched WAC image overlain; (**c**) both a mapped persistent shadow (turquoise) and the stretched WAC image overlain. Arecibo radar was obtained with a range resolution of 1.5 km.

Unnamed O Crater. This crater has a 17 km diameter and is centered at 82° N, 41° E. A dark pattern is exposed on the floor of the crater in a stretched WAC image (Fig. 34a). Overlying radar data aligns strongly with the perimeter of this dark material

(Fig. 34b). The crater's area of persistent shadow also overlaps with these two variables (Fig. 34c). These spatial correlations suggest that the dark pattern revealed on the floor of Unnamed O is a reflectivity-dark, radar-bright deposit, rather than a shadowing effect or image smear.

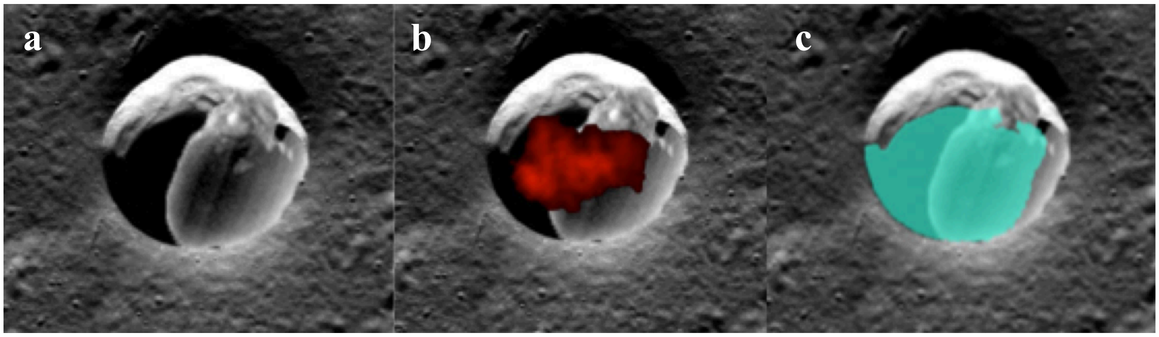

Figure 34. MDIS WAC image of Unnamed O crater (17 km diameter) with: (**a**) a stretched WAC broad-band-filter, 40-ms-exposure image overlain, showing the reflectivity-dark deposit within the crater; (**b**) both Arecibo radar (red) and the stretched WAC image overlain; (**c**) both a mapped persistent shadow (turquoise) and the stretched WAC image overlain. Arecibo radar was obtained with a range resolution of 1.5 km.

Unnamed P Crater. This crater has a diameter of 12 km and is located at 82.9° N, 47.5° E. A stretched WAC image of Unnamed P reveals an intriguing possibly dark deposit in the center of its floor (Fig. 35a). A strong radar signature is returned from the same area that the dark pattern is seen (Fig. 35b). The mapped area of persistent shadow for this crater encompasses the reflectivity-dark and radar-bright deposits (Fig. 35c). The correlations between these three variables suggest that there is a reflectivity-dark deposit on the floor of Unnamed P.

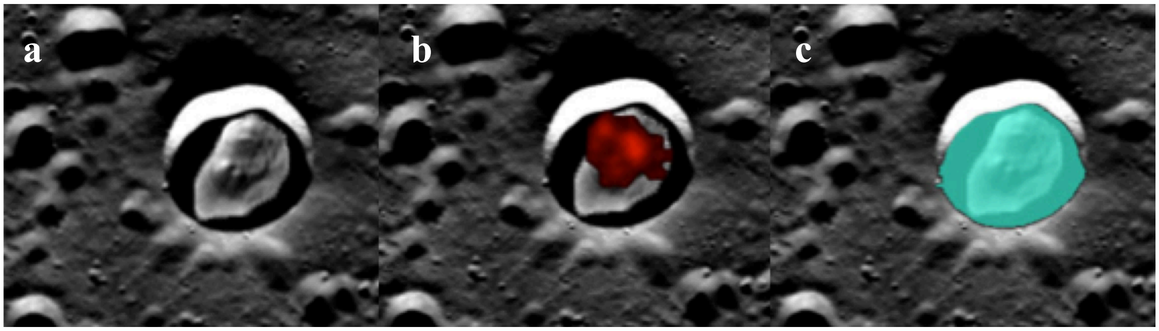

Figure 35. MDIS WAC image of Unnamed P crater (12 km diameter) with: (**a**) a stretched WAC broad-band-filter, 40-ms-exposure image overlain, showing the reflectivity-dark deposit within the crater; (**b**) both Arecibo radar (red) and the stretched WAC image overlain; (**c**) both a mapped persistent shadow (turquoise) and the stretched WAC image overlain. Arecibo radar was obtained with a range resolution of 1.5 km.

Unnamed Q Crater. This 24 km crater is positioned at 83.8° N, 32° E. A stretched WAC image reveals a possible reflectivity-dark deposit on the majority of its floor (Fig. 36a). Overlying radar data shows strong spatial correlation with the dark material, with a notable match along the intricate northern border (Fig. 36b). The area of persistent shadow in Unnamed Q overlays the dark material and radar signature (Fig. 36c). This overlap suggests that the darkness seen in the stretched WAC image is a reflectivity-dark material, as opposed to shadows or image smear.

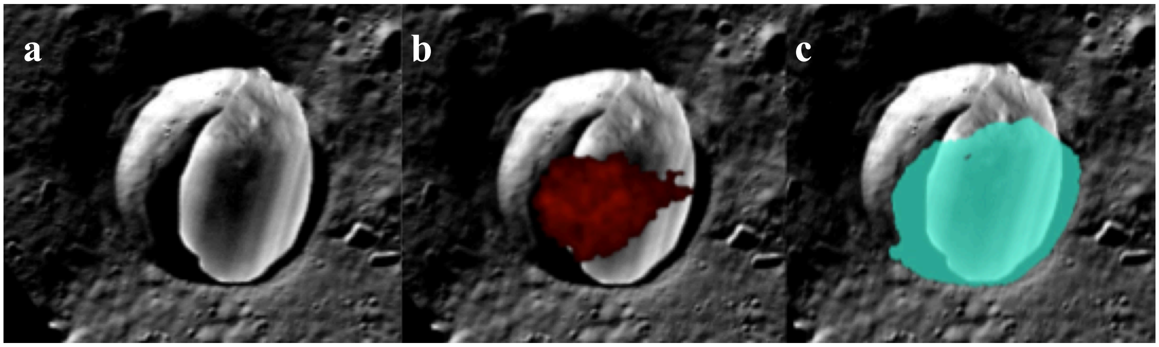

Figure 36. MDIS WAC image of Unnamed Q crater (24 km diameter) with: (**a**) a stretched WAC broad-band-filter, 40-ms-exposure image overlain, showing the reflectivity-dark deposit within the crater; (**b**) both Arecibo radar (red) and the stretched WAC image overlain; (**c**) both a mapped persistent shadow (turquoise) and the stretched WAC image overlain. Arecibo radar was obtained with a range resolution of 1.5 km.

Unnamed R Crater. This crater, with a 8.5 km diameter, is located at 84° N, 219° E. A stretched WAC image of the relatively small crater reveals a possible dark deposit, as seen by the distinct reflectivity difference exposed in the crater's interior (Fig. 37a). Radar data is not strong in this region and no radar signature is returned from this crater (Fig. 37b). An area of mapped persistent shadow encompasses the revealed possible dark material (Fig. 37c). Due to the lack of radar data and strong WAC imagery of this crater, it is unclear whether this crater is a host of a reflectivity-dark deposit. Because craters with a diameter less than or equal to 10 km likely do not provide stable thermal environments for water ice, even with an insulating regolith layer, it is likely the dark spot in Unnamed R is not a sublimation lag insulating water ice (Chabot et al., 2011).

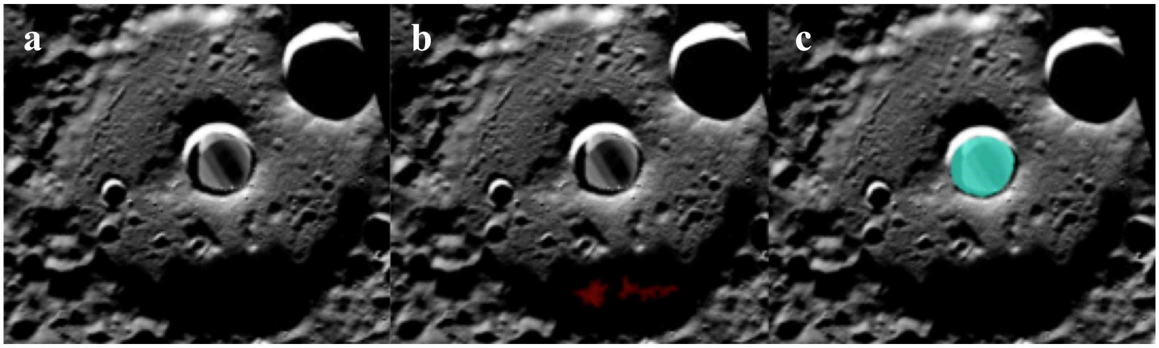

Figure 37. MDIS WAC image of Unnamed R crater (8.5 km diameter) with: (**a**) a stretched WAC broad-band-filter, 40-ms-exposure image overlain, showing the reflectivity-dark deposit within the crater; (**b**) both Arecibo radar (red) and the stretched WAC image overlain; (**c**) both a mapped persistent shadow (turquoise) and the stretched WAC image overlain. Arecibo radar was obtained with a range resolution of 1.5 km.

Unnamed S Crater. This 14 km crater is centered at 85° N, 25° E. The crater's central interior shows a possible reflectivity-dark deposit (Fig. 38a). Radar data of this region overlies the possible dark material (Fig. 38b). Additionally, the mapped area of persistent shadow for Unnamed S conceals the possible dark deposit (Fig. 38c). The spatial correlation between the radar data, persistently shadowed region, and intriguing dark material suggest that the stretched WAC image is revealing a lag deposit, although MLA topographic data would be needed to verify that the exposed dark pattern is not a shadowing byproduct of the crater's central topography.

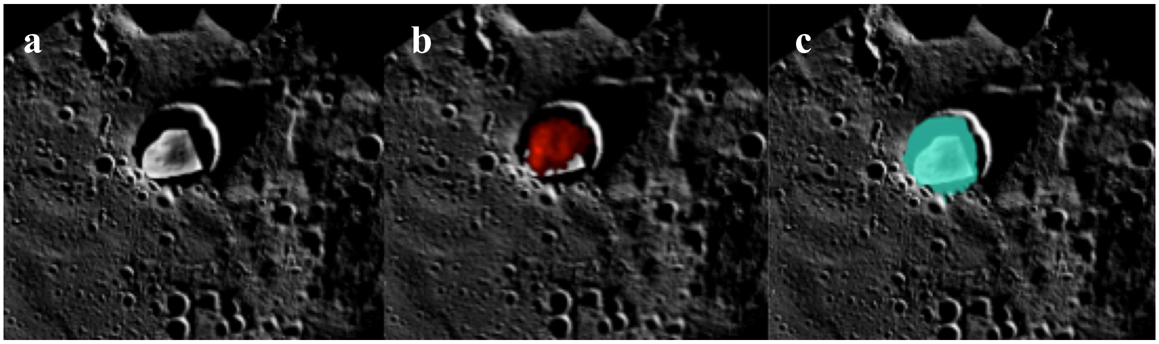

Figure 38. MDIS WAC image of Unnamed S crater (14 km diameter) with: (**a**) a stretched WAC broad-band-filter, 40-ms-exposure image overlain, showing the reflectivity-dark deposit within the crater; (**b**) both Arecibo radar (red) and the stretched WAC image overlain; (**c**) both a mapped persistent shadow (turquoise) and the stretched WAC image overlain. Arecibo radar was obtained with a range resolution of 1.5 km.

Unnamed T Crater. This crater is positioned at 85° N, 175° E and has a 14 km diameter. A small region of Unnamed T's interior is exposed in a stretch WAC image, revealing a possible dark deposit (Fig. 39a). There is not a strong radar signature from this crater, however, the reflectivity differences in the crater align with the perimeter of the crater's persistently shadowed region (Fig. 39b; Fig. 39c). The lack of radar data does not allow us to conclude whether or not the stretched image is revealing an actual dark deposit.

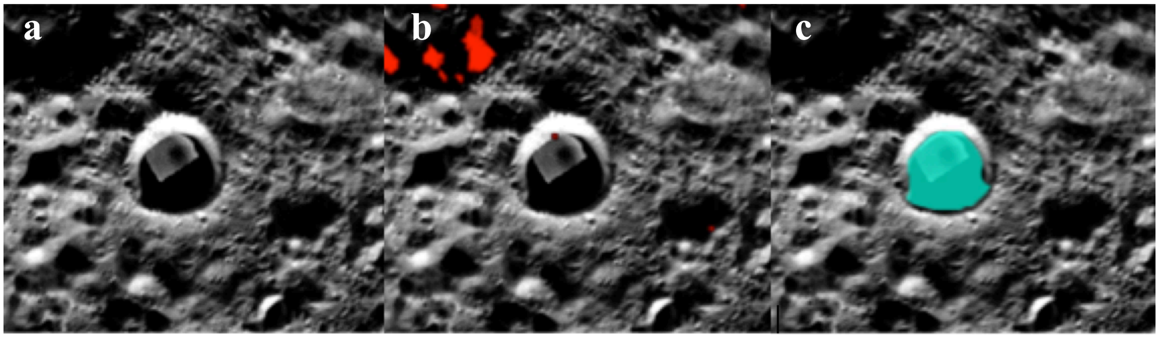

Figure 39. MDIS WAC image of Unnamed T crater (14 km diameter) with: (**a**) a stretched WAC broad-band-filter, 40-ms-exposure image overlain, showing the reflectivity-dark deposit within the crater; (**b**) both Arecibo radar (red) and the stretched WAC image overlain; (**c**) both a mapped persistent shadow (turquoise) and the stretched WAC image overlain. Arecibo radar was obtained with a range resolution of 1.5 km.

Prokofiev Crater. This crater, with a 112 km diameter, is located at 86° N, 63° E. A stretched image of Prokofiev's central interior crater reveals a possible dark deposit

(Fig. 40a). Radar data from this region shows a strong spatial correlation with this dark material, which is completely covered by Prokofiev's region of persistent shadow (40b; Fig. 40c). These spatial alignments suggest that Prokofiev's central interior's crater does host a reflectivity dark deposit. The floor of Prokofiev is also extremely interesting because of a reflectivity difference on its southern floor showing an area of lighter reflectance than the average floor albedo (Fig. 40a). This reflectivity-light deposit aligns extremely well with radar data and is fully encapsulated in Prokofiev's persistently shadowed region (Fig. 40b; Fig. 40c). This reflectivity-light material is interpreted to be a region of exposed surface ice.

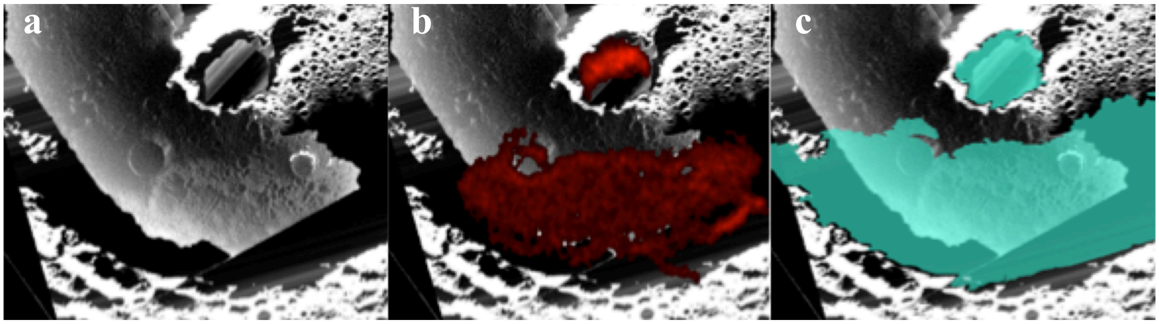

Figure 40. MDIS WAC image of Prokofiev crater (112 km diameter) with: (**a**) a stretched WAC broad-band-filter, 40-ms-exposure image overlain, showing the reflectivity-light deposit within the crater and the reflectivity-dark deposit in the central interior crater; (**b**) both Arecibo radar (red) and the stretched WAC image overlain; (**c**) both a mapped persistent shadow (turquoise) and the stretched WAC image overlain. Arecibo radar was obtained with a range resolution of 1.5 km.

Unnamed U Crater. This crater is positioned at 87° N, 167° E and has a 17 km diameter. Unnamed U hosts a possible dark deposit (Fig. 41a). The radar signature and area of persistent shadow for Unnamed U show strong spatial correlation with the dark material (Fig. 41b; Fig. 41c). These geographical relationships suggest that Unnamed U does host a lag deposit in its interior.

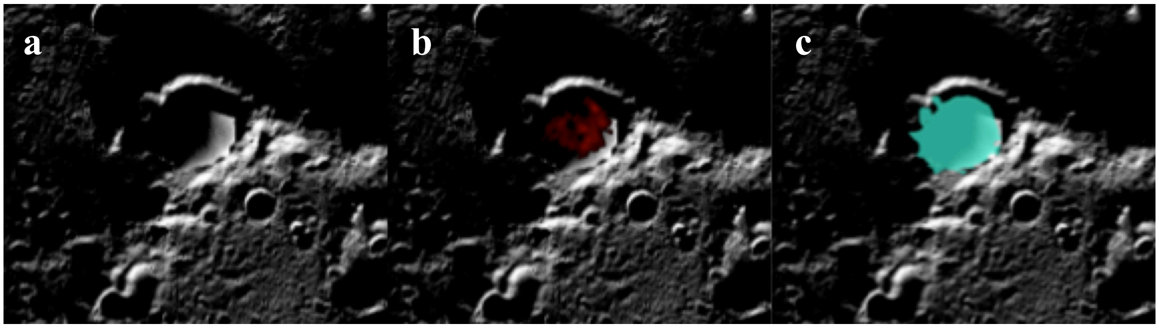

Figure 41. MDIS WAC image of Unnamed U crater (17 km diameter) with: (**a**) a stretched WAC broad-band-filter, 40-ms-exposure image overlain, showing the reflectivity-dark deposit within the crater; (**b**) both Arecibo radar (red) and the stretched WAC image overlain; (**c**) both a mapped persistent shadow (turquoise) and the stretched WAC image overlain. Arecibo radar was obtained with a range resolution of 1.5 km.

Unnamed V Crater. This crater is positioned at 87° N, 190° E and has a diameter of 54 km. The WAC imagery of observation type polar dark crater is poor for this crater. There is a possible dark deposit on Unnamed V's floor, indicated by a possible reflectivity difference along the eastern interior (Fig. 42a). Radar data returns a signature for water ice along the southern floor of the crater (Fig. 42b). Available MESSENGER imagery indicates that the majority of Unnamed V is in persistent shadow (Fig. 42c). It is likely that Unnamed V hosts a reflectivity-dark deposit, although WAC polar dark crater imagery is needed to reveal it.

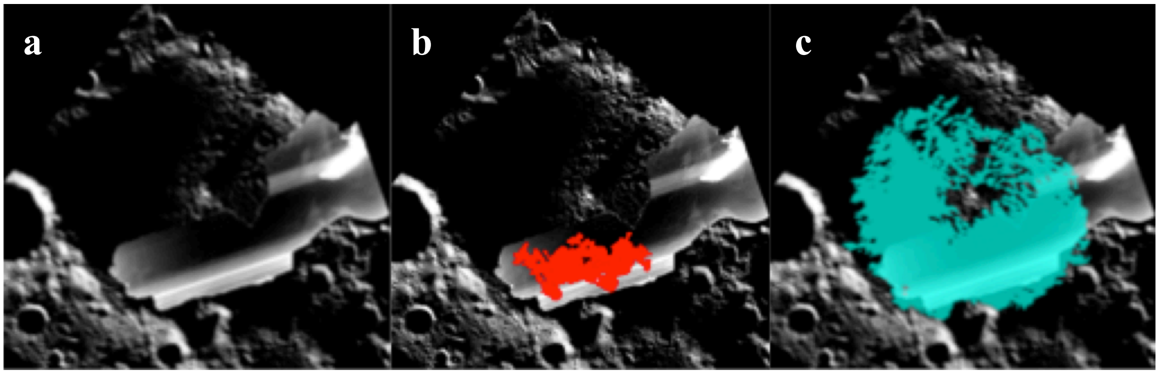

Figure 42. MDIS WAC image of Unnamed V crater (54 km diameter) with: (**a**) a stretched WAC broad-band-filter, 40-ms-exposure image overlain, showing the reflectivity-dark deposit within the crater; (**b**) both Arecibo radar (red) and the stretched WAC image overlain; (**c**) both a mapped persistent shadow (turquoise) and the stretched WAC image overlain. Arecibo radar was obtained with a range resolution of 1.5 km.

Kandinsky Crater. Kandinsky is centered at 78.8° N, 87.9° E and has a diameter of 60 km. A stretched WAC image reveals reflectivity-light material covering the majority of Kandinsky's floor (Fig. 43a). Radar-bright data aligns very well with the light material (Fig. 43b). The entirety of Kandinsky's interior is in persistent shadow (Fig. 43c).

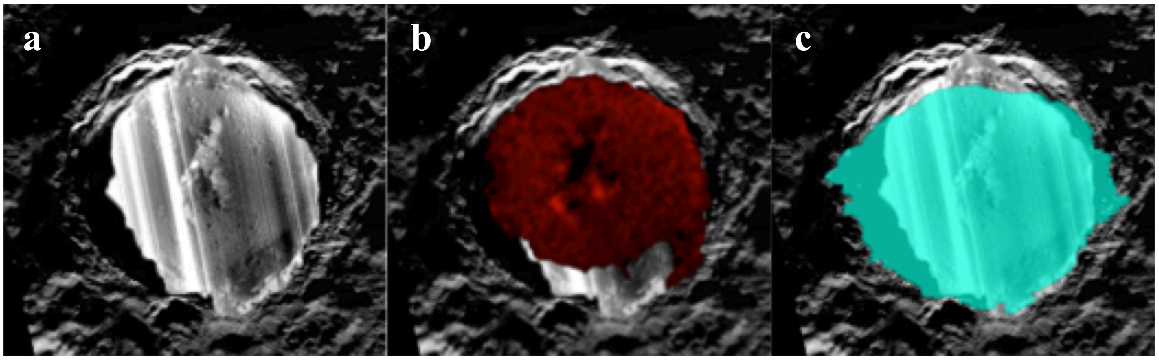

Figure 43. MDIS WAC image of Kandinsky (60 km diameter) with: (**a**) a stretched WAC broad-band-filter, 40-ms-exposure image overlain, showing the reflectivity-light deposit within the crater; (**b**) both Arecibo radar (red) and the stretched WAC image overlain; (**c**) both a mapped persistent shadow (turquoise) and the stretched WAC image overlain. Arecibo radar was obtained with a range resolution of 1.5 km.

Regional Results

In the region 84° N and northward, areas of persistent shadow were determined to cover ~16% of the surface area (Fig. 44). All of the craters in this region are at least partially in persistent shadow. Radar-bright materials are prevalent in this region, covering ~6.7% of the surface area (Fig. 45). The radar data in Figure 45 is the highest-resolution radar image of Mercury's north polar region, with a range resolution of 1.5 km, derived from Arecibo S-band observations at a 12.6 cm wavelength from 1999 through 2005 (Harmon et al., 2011). Radar-bright deposits are present in most of the study area's craters. Radar data is most lacking near the cold pole of 180° E. The majority of craters that did not show radar-bright deposits were less than 10 km in diameter. The two craters above this threshold that did not show radar-bright material were determined through individual analysis to host water ice deposits; despite their lack of radar data the reflectivity-dark deposits revealed on their floors align with mapped regions of persistent shadow. Figure 46 qualitatively shows significant agreement between the spatial distribution of areas of persistent shadow and radar-bright deposits. A quantitative analysis indicates that ~82% of the 2011) radar-bright features in the study area are aligned with the mapped areas of persistent shadow. There is alignment in the spatial distribution of regions of persistent shadow and radar-bright deposits on the floors of nearly every crater with a diameter greater than 10 km. The two craters above this diameter threshold that do not show alignment are lacking in radar data, but as mentioned before, show significant alignment between revealed reflectivity-dark material and areas of persistent shadow in individual analysis. The majority of areas of persistent shadow that are not aligned with radar-bright data are found west of Chesterton. Most radar-bright deposits that are not aligned with persistent shadows cover small spatial extents and are located west of Prokofiev. Many of these radar-bright spots are mapped to small craters.

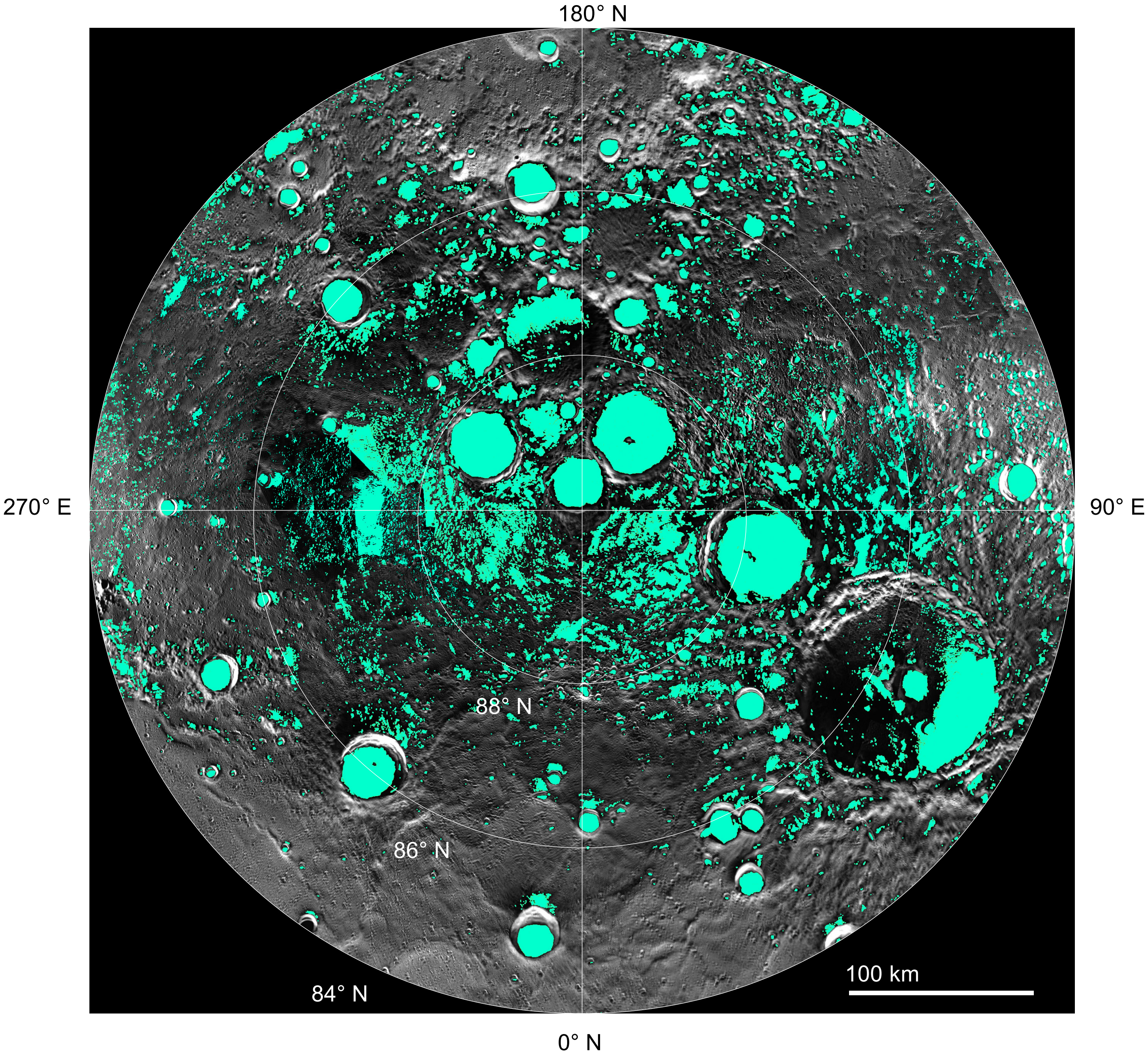

Figure 44. In the region 84° N and northward, areas that are shadowed in all WAC Filter B and G images from MDIS are shown in turquoise on a polar stereographic mosaic of MESSENGER images.

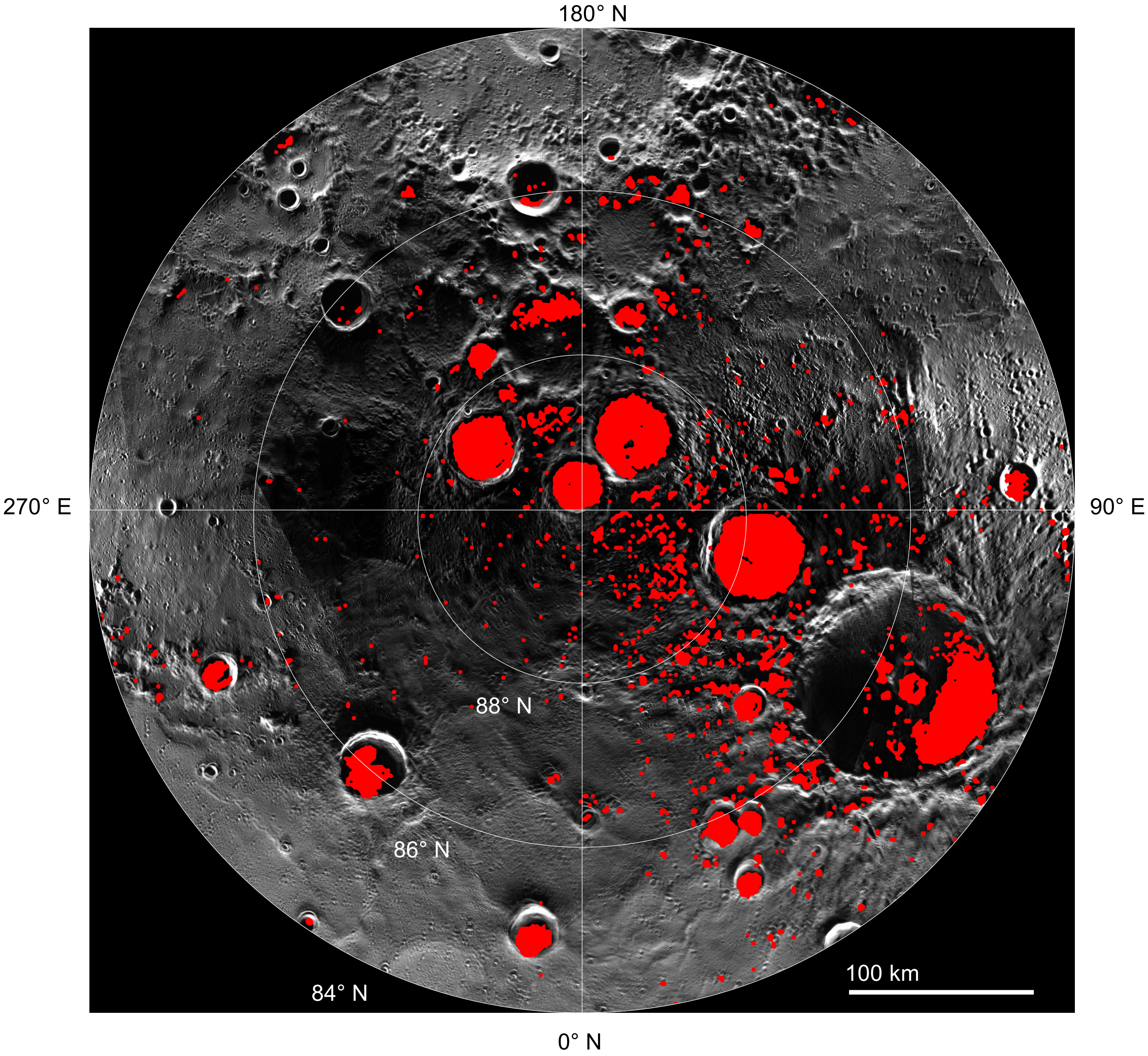

Figure 45. In the region 84° N and northward, an Earth-based radar image from *Harmon et al.* (2011) is stretched to show radar-bright locations in red on a polar stereographic mosaic of MESSENGER images.

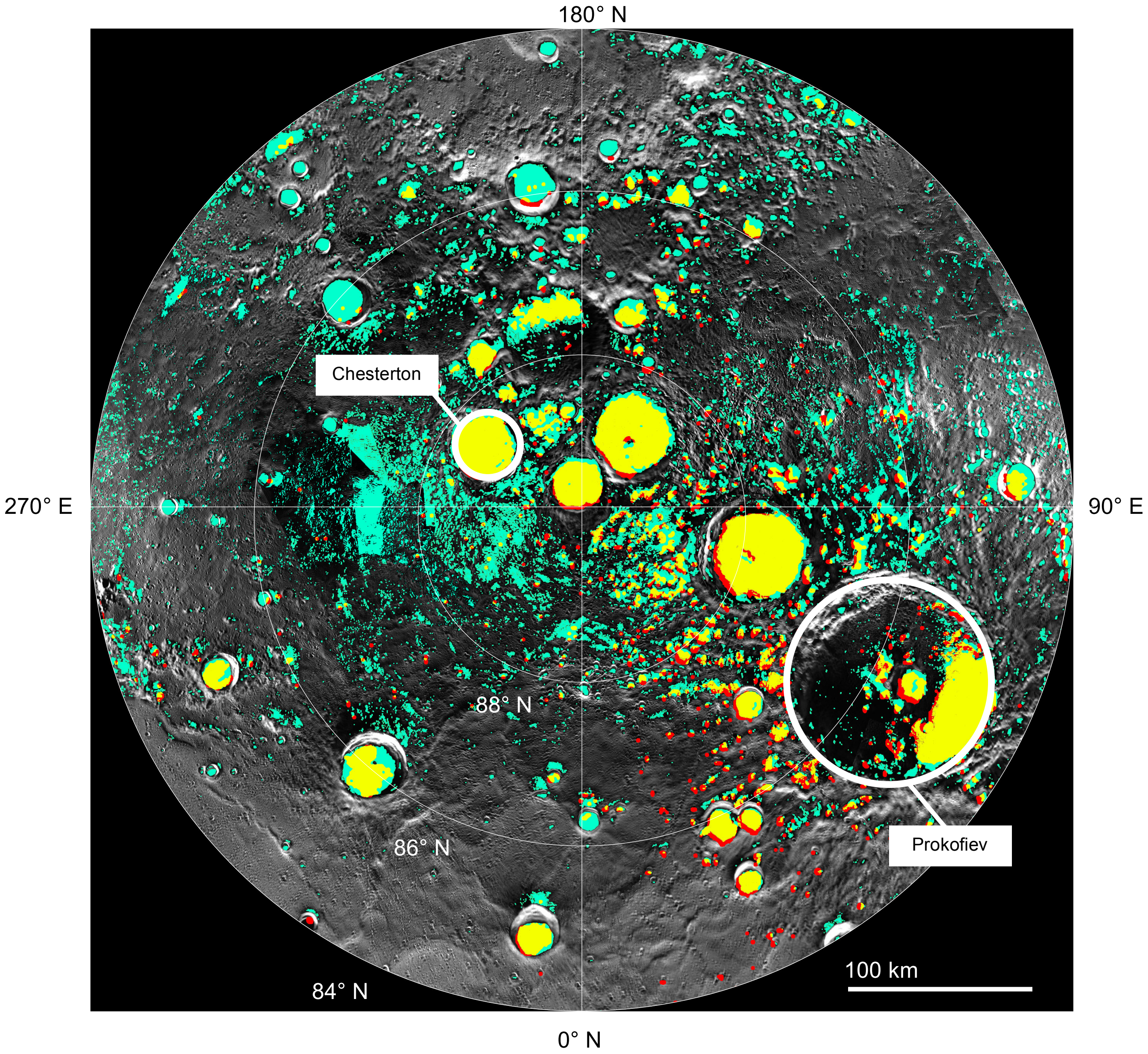

Figure 46. In the region 84° N and northward, locations where turquoise persistently shadowed areas and red radar-bright deposits directly overlap are shown in yellow on a polar stereographic mosaic of MESSENGER images.

Discussion

The 46 individual craters that were identified were originally divided into four groups: craters that hosted definite dark-deposits (30.4%), craters that hosted possible dark deposits (28.3%), craters that did not reveal dark deposits (28.3%), and craters that did not have strong enough imagery for analysis (13.0%). The craters that showed possible dark material were further analyzed for spatial relationships between the possible dark material, radar data, and areas of persistent shadow. Radar data spatially correlated with 84.6% of these craters. The 15.4% lacking spatially correlated data had no significant radar data for their locale, as opposed to showing strong radar data that did not align with possible dark material. These results led to a reclassification of the 45 individually identified craters where 53.2% are interpreted to host reflectivity-dark sublimation lags, 4.2% are interpreted to host reflectivity-light exposed water ice deposits, 29.8% do not reveal dark or light deposits, and 12.8% are unclassified due to the lack of quality WAC images.

When observing the craters that hosted dark material and those that did not, there is an apparent correlation between the crater's central latitude and the presence of dark deposits (Fig. 15). Generally, as latitude increased towards the North Pole, the presence of revealed reflectivity-dark deposits decreased. Higher latitude craters have also shown a correlation with radar-bright deposits. In a previous study, from the 305 identified craters with diameters greater than or equal to 10 km that contain some amount of persistently shadowed area, 92 also host radar-bright deposits (Chabot et al., 2011). The majority of the craters hosting radar-bright deposits have higher central latitudes (Fig. 10). Almost all craters within 10° of the North Pole that have diameters of at least 10 km and persistently shadowed regions also host radar-bright material. Because there is strong radar data for the higher latitude craters, the lack of revealed reflectivity-dark deposits is not evidence to conclude that water ice deposits are absent in these craters. The trend of decreasing revealed reflectivity-dark deposits with increasing latitude may be attributed to two sources: 1) there is less imagery for the regions closest to the pole, thus the probability of finding an image that may be stretched to reveal a dark deposit is slimmer and 2) the regions closest to the pole are home to the most thermally stable craters, which can possibly host water ice exposed at the surface without an insulating sublimation lag (Paige et al., 2013).

Craters with diameters less than or equal to 10 km were not included in this research and previous studies because they are inadequate thermal environments for stable water ice. On Mercury, a transition between simple and complex crater morphologies for primary craters occurs at a crater diameter of ~10 km (Pike, 1988). Simple craters have a bowl-shaped structure that leads to warmer interior temperatures because of indirect heating from scattering and infrared reradiation from crater walls, while complex craters have much flatter floors and do not experience such indirect heating (Vasvada et al., 1999). Thermal studies indicate that primary simple craters with diameters less than or equal to 10 km cannot host water ice on geologic time scales, even with an insulating sublimation lag, because of indirect heating (Chabot et al., 2011).

A quantitative regional analysis indicates that ~82% of the *Harmon et al.* (2011) radar-bright features in the study area are aligned with the mapped areas of persistent shadow. This value is similar to but even greater than the 70% correspondence between radar-bright features and areas of persistent shadow previously studied in the region between 65° N and 85° N (Chabot et al., 2011). The remaining ~30% of the radar-bright features are located either within ~4 km of persistently shadowed regions or within the interiors of small craters (Chabot et al., 2011). Uncertainty in mapping is inherent in the 2 km accuracy of radar positions (Harmon et al., 2011), offset of MDIS mosaics (Becker et al., 2012), and MDIS pixel misregistration (Chabot et al., 2011).

Previous studies of Mercury's shadowed regions calculated that ~1% of the planet's surface between 65° N and 85° N is in persistent shadow, which increases to ~3% for the region 80° N and 85° N (Chabot et al., 2012). These values are similar the determined areas of persistent shadow at Mercury's south polar region at ~2.8% (Chabot et al., 2012), as well as the Moon's south polar region at 4.2% and north polar region at 3.8% (Mazarico et al., 2012). In this study, an analysis of the region 84° N and northward shows that the percentage of persistently shadowed terrain continues to increase to ~16%.

The majority of areas of persistent shadow that are not aligned with radar-bright data are found west of Chesterton (Fig. 46). This area is particularly dark, receiving very little sunlight. It is likely that the area of persistent shadow was overdetermined for this region because the images returned from MESSENGER of this area are inherently very dark, making the threshold between shadowed and non-shadowed terrain very difficult to capture.

Overall, the regional analysis of the region 84° N and northward shows that radar-bright materials near the pole are significantly correlated with persistently shadowed regions, supporting the hypothesis that radar-bright water ice deposits are cold-trapped in Mercury's polar regions. All of the craters in this study area have regions of persistent shadow. Nearly all of the craters with diameters greater than 10 km host radar-bright material. The two craters above this diameter threshold that did not have radar-bright data both revealed reflectivity-dark deposits correlated with regions of persistent shadow in the individual crater analysis, suggesting that water ice may be present under a sublimation lag, although radar data is lacking. Furthermore, previous studies concluded nearly all craters greater than 10 km in diameter within 10 degrees of Mercury's North

Pole were determined to host radar-bright material (Chabot et al., 2012). Together these results suggest that a migration process exists for the radar-bright deposits, allowing radar-bright material to reach all available cold traps.

Polar craters provide an optimal thermal environment as cold traps. First, since these craters are situated in the northernmost, or southernmost, regions of the planet, they typically receive low daily levels of sunlight due to the lack of tilt of Mercury, despite being proximal to the sun. Secondly, the geometric structure of a crater helps prevent sunlight from reaching its interior. The depressed floor and north-facing walls are typically shielded from direct rays due to the obliqueness of the sun striking the surface. The angled rays of the Sun only strike the south-facing walls of high-latitude craters. As warm temperatures are generated on the illuminated rim, very cold temperatures characterize the floor and north-facing walls given the lack of direct sunlight. Thus, polar craters can be as much as 200 K below the temperature of the surface around them, providing stable thermal conditions for hosting the radar-bright material that indicates the presence of water ice (Paige et al., 2013).

Radar-bright material tends to show a pattern of spatial distribution within the interiors of craters. As the central latitude of craters decrease, there is an apparent migration of radar-bright deposits from central crater interior positions to north-facing walls, where sunlight rays do not directly strike. Radar-bright material is almost exclusively found within the bounds of craters.

In a survey of Mercury's radar-bright north polar craters positioned 82° N and equatorward, there was a noted requirement of an insulation layer to protect presumed water ice in the many radar-bright features studied in craters of diameters less than 40 km

(Chabot et al., 2012). This insulation is seen in the results of the individual crater analysis, where a reflectivity-dark layer is spatially correlated with radar-bright material.

It is possible that radar-bright deposits migrate into cold traps through a lengthy evaporation process. If radar-bright material is deposited in a thermally unstable environment, the water likely evaporates from the surface. In a thermally stable environment, however, water can be persistent when it freezes in the crater's interior.

Thermal studies conclude that the cold-trapped water ice in the north polar region is stable from surface sublimation in the billion-year time frame (Paige et al., 2013). The coldest environments of Mercury, which are optimal hosts of the water ice deposits, have low enough temperatures to prevent diffusive mobility of water molecules, keeping it trapped as a stable ice (Schorghofer and Taylor, 2007). In regions of currently stable ground water ice, temperatures are warm enough to allow for diffusive vertical and lateral mobility of water, allowing water to migrate to more thermally stable environments (Siegler et al., 2011). Average temperatures are correlated to the amount of time water ice deposits are thermally stable (Paige et al., 2013). Higher temperatures lead to faster sublimation rates of water ice deposits.

Further thermal stabilization of water ice deposits can occur when a thin layer of organic material acts as insulation. Organic insulation results as an end product of lag deposits. Lag deposits form when comets or water-rich asteroids containing organic compounds impact the planet's surface (Paige et al., 2013). The organic compounds and water composing the impactor disperse and can migrate to the poles where they may become cold-trapped as ices (Paige et al., 2013). As the water in warmer regions vaporizes, the more stable organic compounds are left behind on the surface (Paige et al., 2013). Over time the ice retreats into a stable long-term configuration where the organic impurities and ejecta from the impactor lay above the ice on the surface. These insulating layers are reflectivity-dark, explaining the intriguing reflectivity-dark materials that are seen from stretching MESSENGER WAC images.

Thermal modeling estimates that the radar-bright deposits are thermally stable when buried beneath a ~10 cm-thick layer of ice-free, low-conductivity, organic material (Paige et al., 2013). Available radar data supports these characteristics of the reflectivity-dark insulating material that is revealed in MESSENGER images (Harmon, 2007). These characteristics were derived using the same thermophysical properties as average surface material on Mercury (Vasavada et al., 1999). The sublimation lags found on the surfaces of water ice deposits suggest that the deposits were once more extensive until they receded to their present long-term thermally stable configuration. Since metastable ice deposits must accumulate more rapidly than they sublimate, the formation of the reflectivity-dark sublimation lag deposits can be explained by the episodic impacts of water and other volatiles by comets and asteroids.

While the exact composition of the reflectivity-dark lag deposits is unknown, it is suggested that organic impurities and volatile species comprise these insulating layers. Surface albedo levels are consistent with average surfaces of comets (Sagdeev et al., 1986), asteroids (Gradie and Veverka, 1980; Tedesco et al., 1989), and outer Solar System objects (Cruikshank and Dalle Ore, 2003; Cruikshank et al., 1998). The reflectivity measurements of these bodies are attributed to the presence of macromolecular carbonaceous material, as opposed to space weathering or radiation damage of water ice (Gradie and Veverka, 1980; Cruikshank and Dalle Ore, 2003; Cruikshank et al., 1998). High-energy photons and particles facilitate the processing of simple organic material into the reflectivity-dark macromolecular carbonaceous material exposed at the surface. High-energy particles are abundant in Mercury's polar environment due to the arrangement of magnetic field lines and the pattern of ion precipitation at Mercury's high latitudes (Slavin et al., 2009; Mouawad et al., 2011).

It is likely that comets have contributed significantly to the depositions of water ice on Mercury. Comets are icy planetary bodies that are composed of a solid nucleus, an atmosphere known as a coma, and a tail. The nucleus is the solid core of the comet, comprised of accumulated rock, dust, water ice, and frozen gases such as methane, carbon dioxide, carbon monoxide, and ammonia (Mayo, 1988). Typically, an outer surface of dust and rock amalgamation insulates a predominantly ice body that also has organic constituents, such as methanol, ethanol, ethane, hydrogen cyanide, formaldehyde, hydrocarbons and amino acids (Kuppers et al., 2005; NASA, 2006). The surface crust of comets has low albedo values, just as the dark deposits found in Mercury's polar craters do. The conglomeration of rock fragments and dust consists of complex organic compounds that contribute to the reflectivity-dark properties. The darkness allows the bodies to absorb sufficient heat to fuel outgassing processes. The interior structure of a comet is dominated by water (~90%), but also includes carbon monoxide and carbon dioxide (~9%), and trace amounts (less than 1%) of other volatile species. Comet nucleis are typically 10 km in diameter and contain approximately 80% water by mass. An average comet carries 5×10^{14} kg of water ice (Vanderbilt, 2013). With water having an average density of 1000 kg/m^3, a typical comet was thus calculated to contain an average water volume of 5×10^{11} m^3.

Water can also be introduced to the surface of Mercury by meteorites, although these bodies would contribute significantly less water ice, as they contain only up to 10% water (Vagn, 2975), or 1.81×10^6 to 9.07×10^5 kg of water, derived from the typical meteor size of 1.81 x 10^7 to 9.07 x 10^6 kg (Wylie, 1934). These average mass values were used to derive an average water volume of 1810 to 907 m^3 per meteor. The average water volumes derived for meteors and asteroids represent initial volumes; upon impact, the bodies, and thus the water, will initially be very hot. Impact temperatures cause the majority of water to be lost (Levison et al., 2001). Earth-based radar observations suggest that the radar-bright features of the permanently shadowed polar craters extend to depths of several meters below Mercury's surface (Harmon, 2007). Collisions between comets and other planetary bodies were common in the early Solar System; a significant portion of Mercury's craters may have been caused by comet impacts.

During the Late Heavy Bombardment, which occurred between 3.8 and 4.1 billion years ago, Mercury underwent considerable global resurfacing due to high impact rates (Marchi et al., 2013). During the early stages of the Solar System, the forming planets interacted with leftover material in the dust and gas disk. As the gas giants migrated, small bodies were flung into new orbits, explaining the surge of impacts recorded on Mercury's surface, as well as on Earth's Moon, dating about 700 Ma after the formation of the planets (Gomes et al., 2005). These events possibly deposited much of the water ice and organic debris that are seen on Mercury's poles (Levison et al., 2001).

It is also possible that Mercury's supply of water ice was deposited relatively recently or that an active mechanism for resupply exists (Chabot et al., 2011). The geographic distribution of persistently shadowed craters hosting radar-bright deposits is only bounded by thermal environments, suggesting that the source of radar-bright material or the migration of these materials results in a spatial distribution that allows radar-bright materials to reach all available cold traps (Chabot et al., 2011). The observation that many small craters host radar-bright materials suggests that water ice was deposited relatively recently or that there is an active mechanism for resupply (Chabot et al., 2011). Recent water emplacement was suggested from models of ice burial through regolith emplacement, which concluded that relatively pure water ice insulated by 20 cm of regolith must have been deposited less than 50 My ago (Crider and Killen, 2005).

Reflectivity-dark material was revealed in MESSENGER's WAC images in 30.4% polar craters with central latitudes 75° and northward. We suspect that the 84.6% of craters classified as possibly containing dark material also host reflectivity-dark sublimation lags after analyzing the spatial distribution of possible dark material, mapped persistent shadows, and radar-bright features. Previous work investigated the measurements of surface reflectance made by the spacecraft's MLA at a wavelength of 1064 nm. These measurements revealed that the surface material of radar-bright areas in permanently shadowed north polar craters have approximately half the reflectance value of the average surface reflectance of Mercury (Paige et al., 2013).

In addition, craters Kandinsky and Prokofiev returned reflectance values approximately twice that of the average planetary reflectance (Neumann et al., 2013). These craters were previously calculated to be thermally stable environments for exposed water ice deposits (Fig. 42; Paige et al., 2011). Stretched WAC images did not consistently reveal reflectivity-light deposits of these two craters. Five of 50 Prokofiev images showed reflectivity-light material (Fig. 38a). Only 1 of 48 Kandinsky images showed reflectivity-light material (Fig. 41a). The 45 and 47 images of Prokofiev and Kandinsky, respectively, that did not reveal reflectivity-light material do not, however, dispel the hypothesis that these craters are hosts to reflectivity-light deposits. None of the images returned from MESSENGER revealed reflectivity-dark deposits. Instead, the

WAC images of observation type polar dark crater that are stretched to reveal interior crater surface features are not of high enough quality to show reflectivity differences on the floor. Such quality issues can be attributed to oversaturation and pixel smear. The images that show reflectivity differences together with MLA surface reflectance measurements and thermal stability studies suggest that water ice deposits are exposed at the planet's surface within the crater interiors of Kandinsky and Prokofiev.

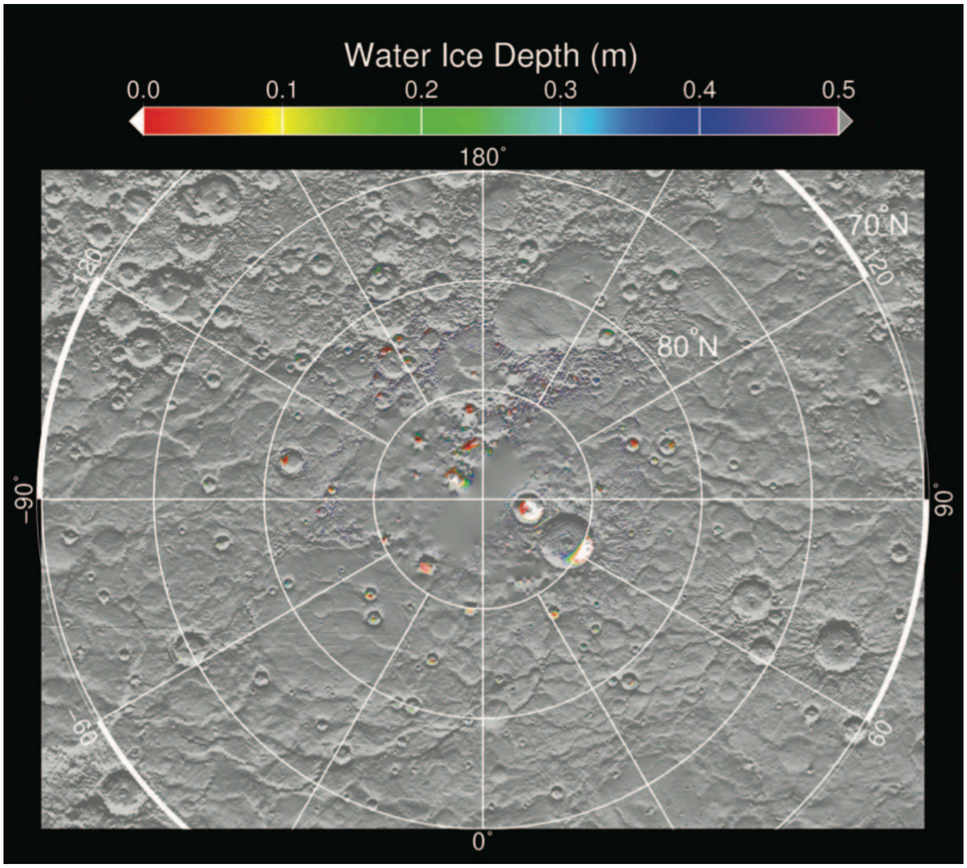

Figure 47. Superposed on a shaded relief map of Mercury's north polar region are the depths below which water ice would sublimate at a rate less than 1 kg per m^2 per Ga. Gray areas represent where subsurface temperatures are too high for cold-trapping of water ice, colored areas indicate the minimum depths at which stable water ice can be buried below the surface, and white areas indicate where water ice can be thermally stable at the surface (Paige et al., 2011).

In previous research, craters positioned 80° N and equatorward were preferentially distributed in the persistently shadowed regions of craters proximal to Mercury's cold-pole longitudes of 90° E and 270° E (Fig. 45). Mercury is known to be in an eccentric orbit with a 3:2 spin-orbit resonance, meaning it rotates on its axis three times for every two revolutions it completes around the sun (Colombo and Shapiro, 1966). This geometry causes the longitudes of 0° and 180° to have warmer mean and maximum annual temperatures due to greater solar insolation and Mercury's eccentric orbit (Siegler et al., 2011).

The evidence for water ice in Mercury's north polar region is very strong with the correlations between radar data, reflectivity measurements, stable thermal temperatures, and now regions of persistent shadow and MESSENGER imagery revealing sublimation lags and even possible exposed ice in two craters. We suspect that these radar anomalies are indeed deposits of water ice, as opposed to another volatile species. MLA surface reflectance measurements, MLA topography measurements, and a ray-tracing thermal model were used to calculate thermal stability of volatile species in the north polar region of Mercury (Paige et al., 2013). Paige et al. (2013) used maximum and average modeled temperatures over a single complete two-year illumination cycle for Mercury's north polar region. At the time of their study, topographic data for the region 84° was incomplete, thus the topography model for this region was extrapolated and provided only estimates. To calculate biannual average surface temperatures, nearly constant subsurface temperatures that exist below the penetration depth of the diurnal temperature wave were used as proxies. For ice-free regolith, this is 0.3 to 0.5 m below the surface, and for ice-rich regions, temperatures can be extrapolated for several meters below the surface (Paige et al., 2013). The results of their study provide strong evidence that the radar-bright features on Mercury are deposits of thermally stable water ice, as opposed to another frozen volatile species, because comparisons between the model-calculated biannual maximum and average temperatures and the thermal stability of candidate volatile species suggest water ice. The radar-bright anomalies in Mercury's polar regions are present in areas where biannual average temperatures do not exceed ~100 K, suggesting that the radar-bright material is not thermally stable above these temperatures (Fig. 43). Between 100 to 115 K, water ice would sublimate into a vacuum in 1 Ga (Paige et al., 2013). Thus the thermal models support the hypothesis of water ice as the composition of the radar-bright deposits, as opposed to another material with a higher or lower volatility.

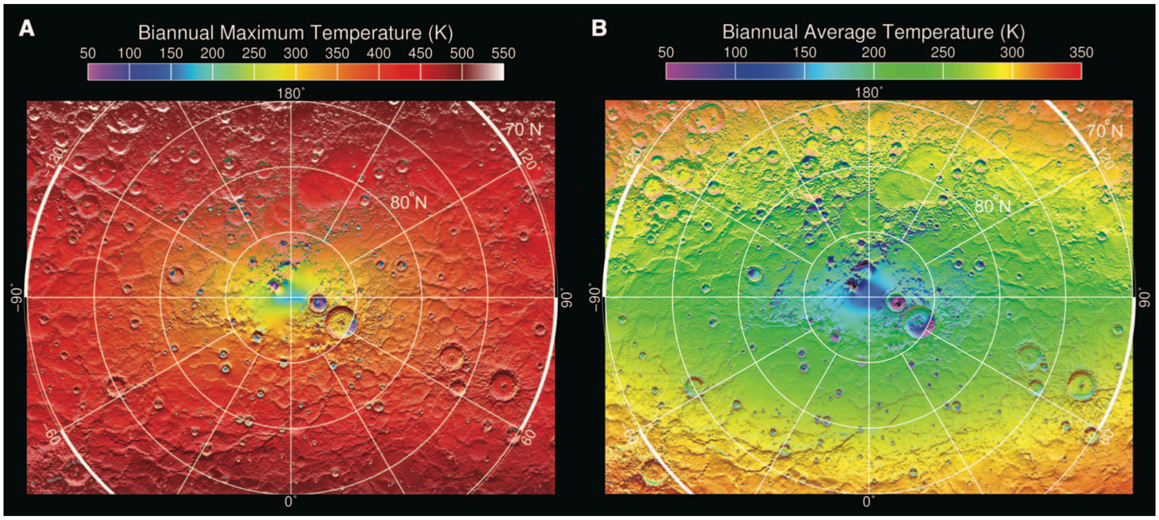

Figure 48. These maps show the calculated **(a)** biannual maximum surface temperatures and **(b)** biannual average temperatures at 2 cm depth superposed on a shaded-relief map of Mercury's north polar region (Paige et al., 2011).

Other volatiles species have also been proposed to compose the radar-bright deposits. Sulfur is an abundant volatile on Mercury that has been suggested as a candidate volatile species (Sprague et al., 1995). For sulfur, however, the fractional areal coverage of radar-bright regions that are of sufficient thermal conditions to trap subsurface elemental sulfur is less than 1 in 500, as compared to the near unity of water results (Paige et al., 2013). While Mercury's polar radar-bright anomalies cannot be interpreted as sulfur-rich, it is possible that cold traps of lower latitudes host sulfur and other volatile species. It is also possible that the water ice deposits in the polar regions contain minor or trace amounts of such less volatile cold-trapped species (Paige et al., 2013).

Conclusion

The evidence for extensive water ice deposits on Mercury's polar regions is strong. Earth-based radar data denote radar-bright deposits in Mercury's north polar region that show the same radar signature expected of pure water ice (Harmon et al., 2011). Neutron spectrometer data indicate hydrogen-rich levels in these polar regions as expected when measuring water molecules (Lawrence et al., 2013). Persistently shadowed craters provide sufficient thermal environments for stable water ice deposits on the time scale of 1 Ga (Paige et al., 2013). Areas of persistent shadow have been mapped in the north polar region and have been shown to correlate with radar-bright features. Finally, imagery of these regions reveals reflectivity-dark material, which we interpret to be sublimation lags that act as thermal insulation for water ice deposits, and reflectivity-light material, which we interpret to be exposed water ice deposits.

Individual analyses of 46 craters located 75° N and northward based on available imagery from MESSENGER revealed a significant spatial correlation between radar-bright regions, reflectivity-dark material, and persistently shadowed areas. 53.2% of the identified craters are interpreted to host sublimation lags that are visible in MESSENGER imagery. 29.8% of the craters do not conclusively reveal sublimation lags in WAC imagery. Finally, 12.8% of the identified craters were in images that were of such poor quality that no analysis could be conducted. Craters that did not reveal reflectivity-dark material may do so as MESSENGER imagery continues to be relayed. These craters cannot be conclusively said to lack reflectivity-dark material, but rather they have no available images that illustrate such material. Imagery of Prokofiev and Kandinsky craters reveals exposed water ice on these craters' surfaces, accounting for the remaining 4.2% of the analyzed craters.

A regional analysis of the polar region 84° N and northward contributes to the evidence that radar-bright materials near the pole are correlated with persistently shadowed regions, closing the data gap that previously existed around this area. All of the craters in this study area have regions of persistent shadow. Nearly all of the craters greater than 10 km in diameter host radar-bright material. The two craters above this diameter threshold that did not have radar-bright data both revealed reflectivity-dark deposits correlated with regions of persistent shadow in the individual crater analysis, suggesting that water ice may be present, although radar data for their region is lacking. Overall, ~82% of the radar-bright features aligned with mapped areas of persistent shadow. The distribution of craters hosting radar-bright materials supports the idea that a source or migration process for the radar-bright material allow it to reach all available thermally stable environments (Chabot et al., 2011).

Understanding Mercury is a fundamental step in studying terrestrial planet formation and evolution because of Mercury's extreme properties. While future NASA missions to Mercury are unforeseen, significant exploration is mounting around Mars. This research of water ice deposits in Mercury's persistently shadowed craters has particular relevance to Mars and its evolutionary history. As human missions to Mars are under development, research teams must be aware of water ice reservoirs on the planet. A major requirement for human landings is that astronauts land proximal to available and obtainable sub-surface water ice (Hoffman and Kaplan, 1997). The demonstrated correlation between areas of persistent shadow, radar-bright material, and reflectivity-dark or -light features can be transferred from Mercury to Mars in the search for water ice.

The evidence for water ice on Mercury is substantial in both quality and quantity. As water ice on the innermost planet is further investigated, it will be interesting to compare the nature of these deposits to that of the polar ice caps on Mars, the Moon, and the icy moons of Jupiter and Saturn. Understanding these water ice reservoirs is essential to understanding the geological, climatic, and conceivably exobiological evolution of these bodies and serves an important role in understanding the evolution of the Solar System at large.

Acknowledgements

Extensive gratitude is owed to many people for the support and guidance that fueled this research. Dr. Nancy Chabot provided invaluable guidance and intellectual inspiration that lead to this project's development and consistently fueled the research. This study would not have been possible without the resources of NASA the Johns Hopkins University Applied Physics Laboratory. Dr. Carolyn Ernst also provided consistent insight during programming phases. And of course, my advisors, Dr. Joel Levine and Dr. Chuck Bailey, are due immeasurable thanks for their constant backing and advice throughout this entire project. I would also like to thank Dr. Heather Macdonald and Dr. Eugene Tracy for serving on my committee.

References

Becker, K.J., Weller, L.A., Edmundson, K.L., Becker, T.L., Robinson, M.S., Enns, A.C., and Solomon, S.C., 2012, Global controlled mosaic of Mercury from MESSENGER orbital images: Lunar Planetary Science, v. 43, abstract 2654.

Bibring, Jean-Pierre, Langevin, Y., Poulet, F., Gendrin, A., Gondet, B., Berthe, M., Soufflot, A., Drossart, P., Combes, M., Bellucci, G., Moroz, V., Mangold, N., Schmitt, B., and the OMEGA team, 2004, Perennial water ice identified in the south polar cap of Mars: Nature, v. 428, p. 627-630.

Cameron, A.G.W., Fegley, B., Benz, W., and Slattery, W.L., 1988, The Strange Density of Mercury: Theoretical Considerations: in Mercury, edited by Vilas, F., Chapman, C.R., and Matthews, M.S., University of Arizona Press, Tucson, Ariz., p. 692-708.

Chabot, N.L., Ernst, C.M., Harmon, J.K., Murchie, S.L., Solomon, S.C., Blewett, D.T., and Denevi, B.W., 2013, Craters hosting radar-bright deposits in Mercury’s north polar region: Areas of persistent shadow determined from MESSENGER images: Journal of Geophysical Research: Planets, v. 118, p. 26-36.

Chabot, N.L., Ernst, C.M., Denevi, B.W., Harmon, J.K., Murchie, S.L., Blewett, D.T., Solomon, S.C., and Zhong, E.D., 2012, Areas of permanent shadow in Mercury’s south polar region ascertained by MESSENGER orbital imaging: Geophysical Research Letters, v. 39, L09204.

Charlier, B., Grove, T.L., and Zuber, M.T., 2012, Composition and differentiation of “Basalts” at the surface of Mercury: Lunar Planetary Science, v. 43, abstract 1400.

Colombo, G. and Shapiro, I.J., 1966, The Rotation of the Planet Mercury: Astrophysical Journal, v. 145, p. 296-306.

Cruikshank, D.P., and Dalle Ore, C.M., 2003, Spectral Models of Kuiper Belt Objects and Centaurs: Earth Moon Planets, v. 92, p. 315-330.

Cruikshank, D.P., Roush, T.L., Bartholomew, M.J., Geballe, T.R., Pendleton, Y.J., White, S.M., Bell, J.F., Davies, J.K., Owen, T.C., de Bergh, C., Tholen, D.J., Bernstein, M.P., Brown, R.H., Tryka, K.A., Dalle Ore, C.M., 1998, The Composition of Centaur 5145 Pholus: Icarus, v. 135, p. 389-407.

Gomes, R., Levison, H.F., Tsiganis, K., and Morbidelli, A., 2005, Origin of the cataclysmic Late Heavy Bombardment period of the terrestrial planets: Nature, v. 435, p. 466-469.

Gradie, J. and Veverka, J., 1980, The composition of the Trojan asteroids: Nature, v. 283, p. 840-842.

Harmon, J.K., 2007, Radar imaging of Mercury: Space Science Review, v.132, p. 307-349.

Harmon, J.K., Perillat, P.J., and Slade, M.A., 2001, High-resolution radar imaging of Mercury's north pole: Icarus, v. 149, p. 1-15.

Harmon, J.K., Slade, M.A., and Rice, M.S., 2011, Radar imagery of Mercury's putative polar ice: 1999-2005 Arecibo results: Icarus, v. 211, p. 37-50.

Hoffman, S.J. and Kaplan, D.I., 1997, Human Exploration of Mars: The Reference Mission of the NASA Mars Exploration Study Team: NASA Special Publication 6107.

Hunten, D.M., Morgan, T.H., and Shemansky, D.E., 1988, The Mercury Atmosphere: in Mercury, edited by Vilas, F., Chapman, C.R., and Matthews, M.S., University of Arizona Press, Tucson, Ariz., p. 562-612.

Ingersoll, A.P., Svitek, T., and Murray, B.C., 1992, Stability of polar frosts in spherical bowl-shaped craters on the Moon, Mercury, and Mars: Icarus, v. 100, p. 40-47.

Kuppers, M., Bertini, I., Fornasier, S., Gutierrez, P.J., Hviid, S.F., Jorda, L., Keller, H.U., Knollenberg, J., Koschny, D., Kramm, R., Lara, L., Sierks, H., Thomas, N., Barbieri, C., Lamy, P., Rickman, H., Rodrigo, R., and the OSIRIS team, 2005, A large dust/ice ratio in the nucleus of comet 9P/Tempel 1: Nature, v. 437, p. 987-990.

Lawrence, D.J., 2012, MESSENGER Finds New Evidence that Water Ice Is Abundant at the Poles of Mercury (in press).

Lawrence, D.J., Feldman, W.C., Goldsten, J.O., Maurice, S., Peplowski, P.N., Anderston, B.J., Bazell D., McNutt R.L., Nittler, L.R., Prettyman, T.H., Rodgers, D.J., Solomon, S.C., Weider, S.Z., 2013, Evidence for water ice near Mercury's north pole from MESSENGER Neutron Spectrometer measurements: Science, v. 339, p. 292-296.

Levison, H.F., Dones, L., Chapman, C.R., and Stern, S.A., 2001, Could the Lunar "Late Heavy Bombardment" Have Been Triggered by the Formation of Uranus and Neptune?: Icarus, v. 151, p. 286-306.

Lucey, P.G., 2013, A Wet and Volatile Mercury: Science, v. 339, p. 282-283.

Marchi, S., Chapman, C.R., Fassett, C.I., Head, J.W., Bottke, W.F., and Strom, R.G., 2013, Global resurfacing of Mercury 4.0-4.1 billion years ago by heavy bombardment and volcanism: Nature, v. 422, p. 59-61.

Mayo, G.J., 1998, Making a comet nucleus: Astronomy and Astrophysics, v. 330, p. 375-380.

Mazarico, E., Neumann, G.A., Smith, D.E., Zuber, M.T., and Torrence, M.H., 2011, Illuminations conditions of the lunar polar regions using LOLA topography: Icarus, v. 211, p. 1066-1081.

Mouawad, N. Burger, M.H., Killen, R.M., Potter, A.E., McClintock, W.E., Vervack, R.J., Bradley, E.T., Benna, M., and Naidu, S., 2011, Constraints on Mercury's Na exosphere: Combined MESSENGER and ground-based data: Icarus, v. 211, p. 21-36.

NASA, Jet Propulsion Laboratory website. http://www.stardust.jpl.nasa.gov/. Accessed 3/1/2014.

Neumann, G.A., 2012, MESSENGER Finds New Evidence that Water Ice Is Abundant at the Poles of Mercury (in press).

Neumann, G.A., Cavanaugh, J.F., Sun, X., Mazarico, E.M., Smith, D.E., Zuber, M.T., Mao, D., Paige, D.A., Solomon, S.C., Ernst, C.M., and Barnouin, O.S., 2013, Bright and dark polar deposits on Mercury: evidence for surface volatiles: Science, v. 339, p. 296-300.

Neumann, G.A., Zuber, M.T., Smith, D.E., and Lemoine, F.G., 1996, The lunar crust: Global structure and signature of major basins: Journal of Geophysical Research, v. 101, p. 16841-16863.

Nimmo, F. and Watters, T.R., 2004, Depth of faulting on Mercury: Implications for heat flux and crustal and effective elastic thickness: Geophysical Research Letters, v. 31, abstract L02701.

Nittler, L.R., Starr, R.D., Weider, S.Z., McCoy, T.J., Boynton, W.V., Ebel, D.S., Ernst, C.M., Evans, L.G., Goldsten, J.O., Hamara, D.K., Lawrence, D.J., McNutt, R.L., Schlemm, C.E., Solomon, S.C., and Sprague, A.L., 2011, The Major-Element Composition of Mercury's Surface from MESSENGER X-ray Spectrometry: Science, v. 333, p. 1847-1850.

Paige, D.A., 2012, MESSENGER Finds New Evidence that Water Ice Is Abundant at the Poles of Mercury (in press).

Paige, D.A., Siegler, M.A., Harmon, J.K., Neumann, G.A., Mazarico, E.M., Smith, D.E., Zuber, M.T., Harju, E., Delitsky, M.L., and Solomon, S.C., 2013, Thermal stability of volatiles in the north polar region of Mercury: Science, v. 339, p. 300-303.

Paige, D.A., Wood, S.E., and Vasvada, A.R., 1992, The thermal stability of water ice at the poles of Mercury: Science, v. 258, p. 643-646.

Pike, R.J., 1988, Geomorphology of impact craters on Mercury: in Mercury, edited by Vilas, F., Chapman, C.R., and Matthews, M.S., University of Arizona Press, Tucson, Ariz., p. 165-273.

Poirier, J.P., 1982, Rheology of ices: a key to the tectonics of the ice moons of Jupiter and Saturn: Nature, v. 299, p. 683-687.

Rasool, S.I., Gross, S.H., McGovern, W.E., 1966, The atmosphere of Mercury: Space Science Reviews, v. 5, p. 565-584.

Sagdeev, R.Z., Blamont, J., Galeev, A.A., Moroz, V.I., Shapiro, V.D., Shevchenko, V.I., and Szego, K., 1986, Vega spacecraft encounters with comet Halley: Nature, v. 321, p. 259-262.

Salvail, J.R. and Fanale, F.P., 1994, Near-surface ice on Mercury and the Moon: A topographic thermal model: Icarus, v. 111, p. 441-455.

Schorghofer, N. and Taylor, G.J., Subsurface migration of H_2O at lunar cold traps: Journal of Geophysical Research, v. 112, E02010.

Siegler, M.A., Bills, B.G., and Paige, D.A., 2011, Effects of orbital evolution on lunar ice stability: Journal of Geophysical Research, v. 116, E03010.

Siegler, M.A., Bills, B.G., and Paige, D.A., 2011, Long Term Climate Variability of Mercury's Poles: Lunar and Planetary Science Conference, abstract 1882.

Slavin, J.A. Acuna, M.H., Anderson, B.J., Baker, D.N., Benna, M., Boardsen, S.A., Gloeckler, G., Gold, R.E., Ho, G.C., Korth, H., Krimigis, S.M., McNutt, R.L., Raies, J.M., Sarantos, M., Schriver, D., Solomon, S.C., Travnicek, P., and Zurbuchen, T.H., 2009, MESSENGER Observations of Magnetic Reconnection in Mercury's Magnetosphere: Science, v. 324, p. 606-610.

Smith, D.E., Zuber, M.T., Phillips, R.J., Solomon, S.C., Hauck, S.A., Lemoine, F.G., Mazarico, E., Neumann, G.A., Peale, S.J., Margot, J., Johnson, C., Torrence, M.H., Perry, M.E., Rowlands, D.D., Goossens, S., Head, J.W., and Taylor, A.H., 2012, Gravity Field and Internal Structure of Mercury from MESSENGER: Science, v. 336, p. 214-217.

Smith, D.E. Zuber, M.T., Phillips, R.J., Solomon, S.C., Neumann, G.A., Lemoine, F.G., Peale, S.J., Margot, J., Torrence, M.H., Talpe, M.J., Head, J.W., Hauck, S.A., Johnson, C.L., Perry, M.E., Barnouin, O.S., McNutt, R.L., and Oberst, J., 2010, The equatorial shape and gravity field of Mercury from MESSENGER flybys 1 and 2: Icarus, v. 209, p. 88-100.

Sprague, A.L., Hunten, D.M., and Lodders, K., 1995, Sulfur at Mercury, Elemnetal at the Poles and Sulfides in the Regolith: Icarus, v. 118, p. 211-215.

Tedesco, E.F., Williams, J.G., Matson, D.L., Weeder, G.J., Gradie, J.C., and Lebofsky, L.A., 1989, A three-parameter asteroid taxonomy: Astronomical Journal, v. 97, p. 580-606.

Thomas, P.G., Masson, P., and Fleitout, L., 1982, Global volcanism and tectonism on Mercury: comparison with the Moon: Earth and Planetary Science Letters, v. 58, p. 95-103.

Vagn, B.F., 1975, Handbook of iron meteorites, their history, distribution, composition, and structure: Center of Meteorite Studies, Arizona State University by the University of California Press, Berkeley, 1409 p.

Vanderbilt Physics website. http://www.vanderbilt.edu/. Accessed 3/1/2014.

Vasavada, A.R., Paige, D.A., and Wood, S.E., 1999, Near-Surface Temperatures on Mercury and the Moon and the Stability of Polar Ice Deposits: Elselvier, v. 141, p. 179-193.

Wylie, C.C., 1934, An Estimate of the Mass of Meteors: Popular Astronomy, v. 42, p. 338-341.

Zuber, M.T., Smith, D.E., Phillips, R.J., Solomon, S.C., Neumann, G.A., Hauck, S.A., Peale, S.J., Barnouin, O.S., Head, J.W., Johnson, C.L., Lemoine, F.G., Mazarico, E., Sun, X., Torrence, M.H., Freed, A.M., Klimczak, C., Margot, J., Oberst, J., Perry, M.E., McNutt, R.L., Balcerski, J.A., Michel, N., Talpe, M.J., and Yang, D., 2012, Topography of the Northern Hemisphere of Mercury from MESSENGER Laser Altimeter: Science, v. 336, p. 217-220.

Zuber, M.T., Smith, D.E., Solomon, R.J., Phillips, R.J., Peale, S.J., Head, J.W., Hauck, S.A., McNutt, R.L., Oberst, J., Neumann, G.A., Lemoine, F.G., Sun, X., Barnouin, O., Harmon, J.K., 2008, Laser Altimeter Observations from MESSENGER's First Mercury Flyby: Science, v. 321, p. 77-79.

Zuber, M.T., Solomon, S.C., Phillips, R.J., Smith, D.E., Tyler, G.L., Aharonson, O., Balmino, G., Banerdt, W.B., Head, J.W., Johnson, C.L., Lemoine, F.G., McGovern, P.J., Neumann, G.A., Rowlands, D.D., and Zhong, S., 2000, Internal Structure and Early Thermal Evolution of Mars from Mars Global Surveryor Topography and Gravity: Science, v. 287, p. 1788-1793.

Tables

Table 1. Craters with definite dark material

Crater Name	Latitude (°N)	Longitude (°E)	Diameter (km)
Unnamed A	75	253	17
Unnamed B	76.7	255	14
Unnamed C	78	97	17
Berlioz	79	39	31
Unnamed D	79.8	356	19
Unnamed E	81	9	12
Unnamed F	81.7	5	16
Unnamed G	81.8	34	17
Unnamed H	82	102	14
Ensor	82	342	26
Unnamed I	82.6	110	24
Remarque	85	354	27
Unnamed J	85.8	188	24
Unnamed K	86	227	28

Table 2. Craters with possible dark material

Crater Name	Latitude (°N)	Longitude (°E)	Diameter (km)
Unnamed L	76	112	19
Unnamed M	79	82	15
Varma	80	341	30
Unnamed N	81	142	34
Unnamed O	82	41	17
Unnamed P	82.9	47.5	12
Unnamed Q	83.8	32	24
Unnamed R	84	219	8.5
Unnamed S	85	25	14
Unnamed T	85	175	14
Prokofiev Center	86	63	21
Unnamed U	87	167	17
Unnamed V	87	190	54

Table 3. Craters with no visible dark material

Crater Name	Latitude (°N)	Longitude (°E)
Unnamed W	79.5	149
Yoshikawa	81	106
Unnamed X	81.8	207.6
Unnamed Y	83	210
Unnamed Z	83.5	225
Unnamed AA	84.6	95
Unnamed AB	85.6	160
Patronius	86	320
Unnamed AC	87	42
Kandinsky	87.8	77.7
Chesterton	88.4	225.5
Tolkein	88.8	149
Tryggvadottir	89	193.5

Table 4. Craters from poor images, preventing any dark material interpretations

Crater Name	Latitude (°N)	Longitude (°E)
Unnamed AD	76	93
Unnamed AE	79.8	35
Unnamed AF	80.8	222
Unnamed AG	85	163
Unnamed AH	86	25
Unnamed AI	86	149

Table 5. Re-classified craters with definite dark material

Crater Name	Latitude (°N)	Longitude (°E)	Diameter (km)
Unnamed A	75	253	17
Unnamed B	76.7	255	14
Unnamed C	78	97	17
Berlioz	79	39	31
Unnamed D	79.8	356	19
Unnamed E	81	9	12
Unnamed F	81.7	5	16
Unnamed G	81.8	34	17
Unnamed H	82	102	14
Ensor	82	342	26
Unnamed I	82.6	110	24
Remarque	85	354	27
Unnamed J	85.8	188	24
Unnamed K	86	227	28
Unnamed L	76	112	19
Unnamed M	79	82	15
Varma	80	341	30
Unnamed N	81	142	34
Unnamed O	82	41	17
Unnamed P	82.9	47.5	12
Unnamed Q	83.8	32	24
Unnamed S	85	25	14
Prokofiev Center	86	63	21
Unnamed U	87	167	17
Unnamed V	87	190	54

Table 6. Re-classified craters with no visible dark material

Crater Name	Latitude (°N)	Longitude (°E)
Unnamed W	79.5	149
Yoshikawa	81	106
Unnamed X	81.8	207.6
Unnamed Y	83	210
Unnamed Z	83.5	225
Unnamed AA	84.6	95
Unnamed AB	85.6	160
Patronius	86	320
Unnamed AC	87	42
Kandinsky	87.8	77.7
Chesterton	88.4	225.5
Tolkein	88.8	149
Tryggvadottir	89	193.5
Unnamed R	84	219
Unnamed T	85	175

Table 7. Craters with light material

Crater Name	Latitude (°N)	Longitude (°E)	Diameter (km)
Prokofiev	86	63	112
Kandinsky	78.8	87.9	60

Appendices

Appendix A. MESSENGER's Payload

Instrument	Primary Use
Mercury Dual Imaging System (MDIS)	A narrow-angle camera (NAC) and a wide-angle camera (WAC) mounted to a pivoting platform provide surface images at a resolution of 250 meters/pixel and images of regions of geologic interest at 25-50 meters/pixel.
Gamma-Ray and Neutron Spectrometer (GRNS)	Surface composition is determined by measuring gamma-ray emissions from the surface by detecting oxygen, silicon, sulfur, iron, hydrogen, potassium, thorium, and uranium levels to a depth of 10 cm.
X-Ray Spectrometer (XRS)	X-ray spectral lines from magnesium, aluminum, sulfur, calcium, titanium, and iron are detected in the 1-10 keV range to determine the mineral composition of the surface.
Magnetometer (MAG)	The strength and average position of the magnetic field is measured.
Mercury Laser Altimeter (MLA)	The altimeter detects the light of an infrared laser as light reflects off the surface, measuring the topography of Mercury.
Mercury Atmospheric and Surface Composition Spectrometer (MASCS)	The spectrometer measures the reflectance of infrared light to determine levels of iron- and titanium-bearing minerals on the surface and measures ultraviolet light emissions to study Mercury's tenuous atmosphere.
Energetic Particle and Plasma Spectrometer (EPPS)	An Energetic Particle Spectrometer (EPS) measures charged particles in the magnetosphere and a Fast Imaging Plasma Spectrometer (FIPS) measures the charged particles from the surface.
Radio Science (RS)	Spacecraft positioning data is used to measure the gravity of Mercury and the state of the core.

Appendix B. Explanation of MESSENGER Acronyms

Acronym	Term	Description
MESSENGER	Mercury Surface, Space Environment, Geochemistry, and Ranging	Spacecraft orbiting Mercury
MDIS	Mercury Dual Imaging System	Imagining system mounted on MESSENGER composed of two cameras
WAC	Wide-Angle Camera	Camera with 10.5° by 10.5° field of view that can image in 11 different filters and monochrome
NAC	Narrow-Angle Camera	High resolution camera with 1.5 ° by 1.5° field of view that images in black and white
ISIS	Integrated Software for Images and Spectrometers	Software used to manipulate spacecraft data received from MESSENGER
EDR	Experimental Data Record	Collection of MESSENGER data

Appendix C. ISIS3 Tools Used

Tool	Use
mdis2isis	Import MESSENGER/MDIS EDR/RDR products into ISIS cubes
spiceinit	Determine SPICE kernels for a camera cube
mdiscal	Calibrates MESSENGER/MDIS EDR/RDR products
trim	Trim edges of input cube
cam2map	Convert camera image to a map projection
map2map	Modify a cube's map projection
isis2std	Export a cube to a PNG, BMP, GIF, TIFF, JPEG, or JPEG 200
automos	Create a mosaic using a list of map projected cubes
fx	Generalized arithmetic operation using multiple cube files
mask	Set pixels to NULL using a mask cube